



**NUMERICAL SOLUTIONS TO THE
TWO DIMENSIONAL BOLTZMANN EQUATION**

THESIS

Christopher G. Smithtro, Captain, USAF

AFIT/GAP/ENP/99M-13

**DEPARTMENT OF THE AIR FORCE
AIR UNIVERSITY
AIR FORCE INSTITUTE OF TECHNOLOGY**

Wright-Patterson Air Force Base, Ohio

19990402 031

**NUMERICAL SOLUTIONS TO THE
TWO DIMENSIONAL BOLTZMANN EQUATION
THESIS**

Christopher G. Smithtro, Captain, USAF

AFIT/GAP/ENP/99M-13

Approved for public release; distribution unlimited

The views expressed in this thesis are those of the author and do not reflect the official policy or position of the Department of Defense or the U.S. Government.

**NUMERICAL SOLUTIONS TO THE
TWO DIMENSIONAL BOLTZMANN EQUATION**

THESIS

Presented to the Faculty of the Graduate School of Engineering
of the Air Force Institute of Technology

Air University

Air Education and Training Command

In Partial Fulfillment of the Requirements for the
Degree of Master of Science in Applied Physics

Christopher G. Smithtro, B.S.

Captain, USAF

March 1999

Approved for public release; distribution unlimited

**NUMERICAL SOLUTIONS TO THE
TWO DIMENSIONAL BOLTZMANN EQUATION**

Christopher G. Smithtro, B.S.

Captain, USAF

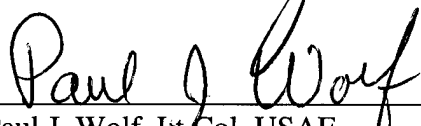
Approved:



William F. Bailey, Ph.D.
Chairman, Research Committee

24 Feb 99

Date



Paul J. Wolf, Lt Col, USAF
Member, Research Committee

24 FEB 99

Date



David E. Weeks, Ph.D.
Member, Research Committee

24 Feb 99

Date

Acknowledgements

The last few months have certainly been hectic, and I would like to acknowledge those who have helped me through it. Special thanks goes to my advisor Dr. Bailey, whose ability to see the forest from the trees regularly saved me from heading down the path to oblivion. Never once did I see him snicker, even though I'm sure many of my questions were ridiculous. Also to Eric Bennett on whose work much of this thesis is based, without his solid development I'd still be floundering in a C of code. And of course to my wife Sally, for having the foresight to go TDY to Saudi Arabia for the majority of the research period, leaving me with an empty house and no distractions. I am also grateful to the Major Shared Resource Center who provided not only much needed super computing time, but also patient solutions to my innumerable UNIX problems.

Christopher G. Smithtro

Table of Contents

	Page
Acknowledgements	iii
List of Figures	vi
List of Tables.....	viii
List of Symbols and Abbreviations	ix
Abstract	xi
I. Introduction.....	1
II. Background.....	4
2.1. Introduction to the Positive Column	4
2.1.1. Glow Discharge Basics	4
2.1.2. Modeling the Glow Discharge	9
2.2. The Local Approximation	12
2.3. The Nonlocal Approximation	14
III. Methodology of the Strict Kinetic Solution	17
3.1. Theoretical Development of Solution Equations	17
3.1.1. Expansion of the Collisional Boltzmann Equation	17
3.1.2. Discussion of Collision Terms	22
3.1.3. Boundary Conditions to the Solution Equation	26
3.2. Numerical Method of Solution.....	31
3.2.1. Forming the Solution Grid	33
3.2.2. Finite Differencing on the Non-Uniform Grid.....	36
3.2.3. Solving the Sparse Banded Matrix.....	38

IV. Implementation of the Strict Kinetic Solution	42
4.1. Phase I: Radially Homogeneous System.....	42
4.2. Phase II: Include Radial Potential	43
4.3. Phase III: Add Source and Loss Terms	45
4.4. Phase IV: Completion of the Model.....	49
V. Model Validation.....	51
5.1. Exposition of Model Output and Comparison to Uhrlandt and Winkler Results	51
5.2. Verification Against the Local and Nonlocal Approximations.....	57
5.3. Comparison to Monte Carlo Methods Using Argon	59
VI. Investigation of Special Topics.....	62
6.1. Current Flow within the Solution Space	62
6.2. Applicability of the Approximate Methods	65
6.3. Effect of the Wall Loss Boundary Condition.....	68
VII. Conclusions and Recommendations	72
7.1. Conclusions	72
7.2. Recommendations for Future Work	74
Appendix A Macroscopic Quantities Derived from the Distribution Function	77
Appendix B Derivation of Strict Solution Equations.....	79
Appendix C Derivation of Upper Boundary Condition	86
Appendix D Boltzmann Equation in Finite Differenced Form.....	88
Bibliography.....	93
Vita.....	95

List of Figures

	Page
Figure 1 Schematic of a typical neon discharge in a 50 cm tube at 1 Torr. Luminous regions are shown shaded, along with plots of luminosity, electric field, and charge density [4, pg 399].	5
Figure 2 Experimentally determined radial potential ($-V[r]$ in Volts) as a function of normalized radius for neon and krypton at .62 and 4.8 Torr respectively [7].	8
Figure 3 Four examples of the electron energy distribution function plotted on a log/linear scale: (a) Maxwellian, (b) Druyvesteyn, (c) typical Noble Gas, (d) typical Molecular gas.....	9
Figure 4 Energy level diagram depicting three types of inelastic electron collisions involving neutral species k and excited states l and l'	22
Figure 5 Electron scattering in three types of inelastic electron collisions.....	23
Figure 6 Diagram of typical solution area including the four boundaries. Boundaries (2)-(4) are determined at run-time by the input conditions.....	26
Figure 7 Comparison of the two types of wall loss boundary conditions.....	30
Figure 8 Diagram of basic parameters used in forming the solution grid.....	32
Figure 9 A schematic of the grid in i/j space. Solution points, m , are numbered sequentially from 1 to DIM	35
Figure 10 Sparse Banded Matrix in traditional storage (a) and reduced storage (b) as required by DGBSV routine. Zero elements are not shown.	39
Figure 11 Log/linear plots of the EEDF versus total energy at five neighboring radial bins demonstrating the effect of a volumetric point gain/loss in the local (a) and nonlocal (b) regimes. The plots are vertically offset in order to distinguish differences between them.	46

Figure 12 Log/linear plot of the EEDF versus energy for the case of a point source and an uninterrupted line-of-losses within the 2-D strict model. Model output is also equivalent to the result of a 1-D model with a single point loss. Dashed lines show undisturbed Druyvesteyn distributions.	48
Figure 13 Log/linear plot of components of the EEDF, for the neon discharge at two radii, calculated using the strict solution: isotropic - $f_0[r,u]$, radial - $f_r[r,u]$, and axial - $f_z[r,u]$	53
Figure 14 Terms in the electron particle balance as a function of radius for the case of a neon discharge.	55
Figure 15 Important terms in the local energy balance as a function of radius for the neon discharge. Not shown are elastic collisional losses and inelastic collisional gains, which are insignificant in this case.	56
Figure 16 Comparison (a) of Monte Carlo calculation [9] (left) and strict solution, present work, (right) for an argon column at three different radii. Plotted is the EEDF as a function of total energy.	60
Figure 17 Comparison (b) of Monte Carlo calculation [9] (left) and strict solution, present work, (right) for an argon column at three different radii. Plotted is the EEDF as a function of total energy.	61
Figure 18 Vector diagram of electron flux within the neon discharge solution area.	63
Figure 19 Integrated current flows within the neon discharge, plotted as a function of the tube radius.	64
Figure 20 Comparison of the on-axis EEDF for the wall loss cone (dashed) and wall loss function (solid) at two PR values: (a) $PR = 1.0$ and (b) $PR = 0.1$	69
Figure 21 Isotropic component of the EEDF at $r = R_{\text{wall}}$ for three different values of the wall loss function parameter a	70

List of Tables

	Page
Table 1 Electron/Atom and Atom/Atom Collision Data Used in Neon Discharge Calculations. Notation: <i>m</i> – metastable, <i>r</i> – resonance, <i>o</i> – ground state.....	52
Table 2 Input parameters for model comparisons between Monte Carlo and strict solutions in an argon column.	60
Table 3 Range of validity for models of interest [8, pg 5943].	65
Table 4 Deviation from nonlocality (relative percent) for a neon column as a function of <i>PR</i> value and radius.	66
Table 5 Deviation from nonlocality (relative percent) for an argon column as a function of <i>PR</i> value and radius.	67
Table 6 Deviation from locality (relative percent) for a neon column as a function of <i>PR</i> value and radius.	68

List of Symbols and Abbreviations

CBE	Collisional Boltzmann Equation
dc	Direct Current
<i>DIM</i>	Total number of points in the solution grid
F	Complete electron distribution function, normalized to one
F_0	Isotropic component of electron distribution, normalized to one
f	Complete electron distribution function, normalized to the electron density
f_0	Isotropic component of electron distribution function
\vec{f}_1	Anisotropic vector component of electron distribution function, includes f_r and f_z
f_r	Anisotropic radial component of electron distribution function
f_z	Anisotropic axial component of electron distribution function
EEDF	Electron Energy Distribution Function
EVDF	Electron Velocity Distribution Function
e	Elementary charge of an electron (magnitude)
ε	Total energy
ε_{\max}	Maximum total energy in the solution space
E_r	Radial electric field
E_z	Axial electric field
Gb	Gigabyte
i	Radial bin index
j	Energy bin index
LU	Lower/Upper, as in LU decomposition of a matrix
m	Electron mass

M_N	Neutral mass
NI	Number of radial bins in the solution space
NJ	Number of energy bins in the solution space
$n_e[r]$	Electron density
ODE	Ordinary Differential Equation
$\phi[r]$	Negative of radial potential, $V[r]$, or electron motive
$\Delta\phi$	Jump in radial potential which occurs at the wall in the loss cone formalism
PR	Pressure \times Radius value. Used to quantify the energy relaxation length requirement
P	Pressure
PDE	Partial Differential Equation
Q	Collisional cross section
r	Radial position
R_{wall}	Radius of tube wall
u	Kinetic energy
v	Speed
$V[r]$	Radial potential
χ	Reflection coefficient in loss cone formalism
z	Rate coefficient of Penning electron production

Abstract

A strict kinetic, two-dimensional model of the electron kinetics within a glow discharge positive column is developed. The problem is solved in cylindrical geometry using the standard two-term Legendre expansion of the electron velocity distribution function. The model establishes a steady state solution, such that the net ionization rate is exactly balanced by the wall loss. In addition to a thorough analytic development, we present the numerical techniques used to solve the resulting elliptic partial differential equation, including an efficient method to treat sparse banded matrices. The model is validated against published results, local and nonlocal kinetic approximations, and a previous Monte Carlo treatment. Having created a working model, we conduct an investigation into current flow within the solution area of a neon column, made possible by this 2-D treatment. Furthermore, we investigate the range of applicability of the earlier local and nonlocal kinetic approximations and finally present a short discussion on the effect different forms of wall loss have on the overall distribution function.

Numerical Solutions to the Two Dimensional Boltzmann Equation

I. Introduction

Based on its ubiquitous application in neon and florescent lamps, and more recent use in electric discharge lasers, one might expect the underlying glow discharge phenomenon to be thoroughly understood and computationally well modeled. We must, of course, have an accurate model of these devices in order to optimize their design efficiency. However, until recently, none of the available models accurately depicted the often dramatic effect of radial inhomogeneities within the glow discharge device. This research addresses and resolves that deficiency by implementing the latest modeling technique – a two-dimensional solution of the collisional Boltzmann equation (CBE), which we call the strict kinetic solution¹.

Prior to the strict solution, most researchers relied on two approximate kinetic methods. These solution methods, known as the local and nonlocal approximations, solve the CBE in the limit of high and low pressure, respectively. Until the 1970s the local (high-pressure) approximation was used almost exclusively, even though the assumptions were inherently incorrect in most realistic situations. In the past twenty years the nonlocal approximation gained favor as a more realistic model for low-pressure

plasmas. Yet most of the experimental and commercial devices in use today operate in a parametric regime between the two where neither the local or nonlocal approximation is valid.

Recent advances in computing power have facilitated the use of a strict kinetic solution that solves the complete CBE in two dimensions. By avoiding the assumptions inherent to the approximate methods, the strict solution is able to accurately treat spatial inhomogeneities and remain valid across a broad spectrum of pressures. The strict solution is in fact the most rigorous kinetic treatment available today.

While the strict solution is an invaluable tool to probe the kinetics of the glow discharge, the Air Force is interested in it primarily as a first step toward much more lofty goals. Soviet research, extending over the past twenty years and summarized by Hilbun [1], has revealed anomalous shock structure and wave propagation in the presence of weakly ionized gases. These results recently spurred experimental investigations in the U.S. that have confirmed the Soviet findings [2, 3]; they include a reduction in shock strength, increased shock standoff distance, and a general broadening of the shock structure. Understanding and application of these phenomena could lead to a new class of hypersonic vehicles that utilize plasma effects to generate shocks characteristic of one half the true Mach number with a correspondingly significant decrease in vehicle drag! However, prior to designing a futuristic hypersonic fighter, we must thoroughly explore the plasma-aircraft interaction. This necessitates a refined plasma modeling capability that is able to solve the CBE in at least two dimensions. Furthermore, the model must be

¹ The term "kinetic" refers to any technique that solves the CBE directly. "Strict" refers to solving the

benchmarked in a parametric regime where extensive experimental data are available; the glow discharge satisfies this requirement. With this goal in mind, the strict solution detailed in this thesis represents a first generation of the required modeling capability.

Optimistic extrapolations aside, the main focus of this research is to develop, implement, and test a numerical solution to the spatially inhomogeneous CBE – the strict kinetic solution. As such, the body of this thesis focuses on the theoretical and numerical framework behind the strict solution, as well as the specific details of the model. The remaining chapters follow the model through its background, development, implementation, and validation.

Chapter II covers background material leading to the strict solution. It specifically discusses the physics of the glow discharge, as well as giving a brief summary of the techniques and approximations previously used to model it. In Chapter III, we develop the strict solution method; the first half covers a theoretical treatment of the relevant equations, while the second discusses the numerical techniques used to solve them. The model takes shape in Chapter IV; here we present “status checks” at four phases of development, using analytic equations and physical reasoning to establish the solution’s validity and accuracy. The next chapter is devoted to a validation of the complete model, comparing our solution to others. Chapter VI includes a short investigation into some interesting topics made possible by the strict solution. Finally, the last chapter discusses my ideas for future work, considering both expansion of the current model and modifications to treat related subjects.

CBE completely, avoiding the local or nonlocal approximations.

II. Background

Elementary physics of the direct current (dc) glow discharge² is the subject of numerous textbooks (see Nasser [4] and Howatson [5]), and we can only briefly review the basic concepts here. The first section in this chapter is an introduction to the glow discharge and the positive column in particular. The following two sections look more closely at previous kinetic approximations used to model the positive column and discuss their assumptions and range of applicability.

2.1. Introduction to the Positive Column

2.1.1. Glow Discharge Basics

A simple glow discharge device consists of a cylindrical glass tube, filled with a gas (see Figure 1). Most tubes are one to two centimeters in diameter, and between ten and one hundred centimeters long. Within the tube, the gas pressure normally ranges from a few hundredths to tens of a Torr. The discharge is initiated and sustained by an external dc power supply. The discharge voltage is typically several hundred Volts, with corresponding currents of tenths to hundreds of milli-amperes [6]. The power is coupled to the plasma through two electrodes, one at each end of the tube.

In very simple terms, the glow discharge is created as the externally provided power is converted into light and heat. The conversion occurs when electrons, accelerated by the applied axial electric field, collide with the neutral gas. Some of these

² This study considers only the direct current discharge. Suitable modifications to the model would allow us to account for an alternating current as well.

energetic electrons have enough energy to excite the neutrals into higher electronic states. These neutrals in turn emit radiation as they relax to the ground state. This radiation is the glow.

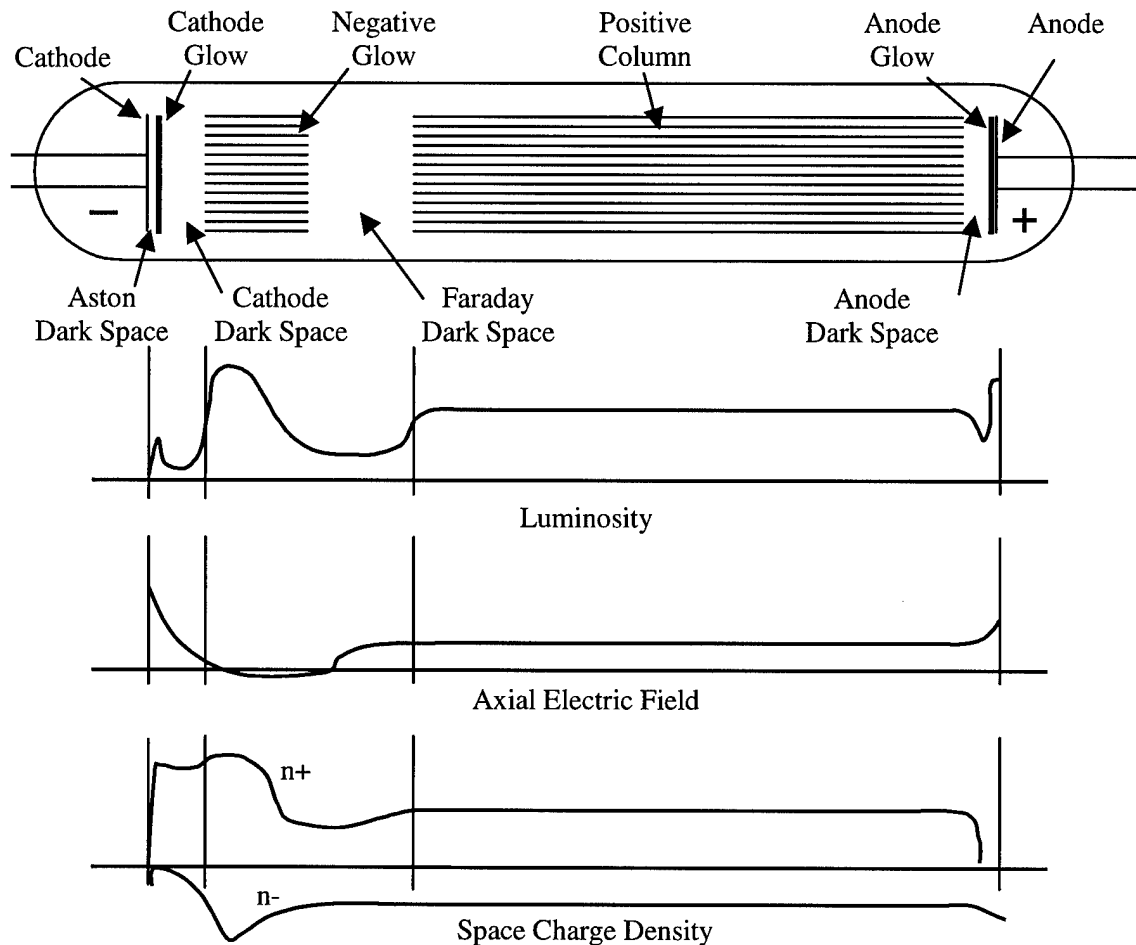


Figure 1 Schematic of a typical neon discharge in a 50 cm tube at 1 Torr. Luminous regions are shown shaded, along with plots of luminosity, electric field, and charge density [4, pg 399].

Figure 1 illustrates a schematic of a typical glow discharge device, as well as relative values of important parameters along the length of the tube. Studying the figure, we note that the glow discharge can be divided into a number of physically meaningful regions [4, pp 397-425]. At the cathode end, the impact of heavy ions onto the cathode surface releases electrons into the system. At the time of their release, the electrons do

not have enough energy to excite electronic levels in the neutrals; hence there is no radiative decay and no glow emission in this region, known as the Aston Dark Space.

The strong axial electric field accelerates the freed electrons toward the anode, and their kinetic energy soon exceeds the excitation threshold of the neutral species. This marks the beginning of the Cathode Glow. Note that in this region the luminosity is still quite low, since the number of electrons is relatively low. The electrons continue to accelerate, achieving energies in excess of the neutral's ionization threshold at the Cathode Dark Space boundary. When this occurs, ionization begins to compete with excitation for electron energy, reducing the overall luminosity. The luminosity does not go to zero however; in fact all the dark regions have some luminosity, just at a lower level than their neighbors.

The electrons released by ionization in the Cathode Dark Space are accelerated to excitation energies, and because of the increase in electron density, the Negative Glow is the brightest band in the entire tube. The large number of electrons in this region causes a weakening in the axial field strength, and it can actually reverse for a short distance [4, pg 412]. Because of the weak field, the acceleration in this region is not strong enough to keep the electrons above the excitation threshold, and the Faraday Dark Space results. In the Faraday Space, the number of electrons tapers off, and the axial electric field increases, until it is once again able to accelerate electrons to excitation energies.

At this point, the Positive Column begins, maintaining a nearly uniform glow. Near the end of this column, the axial field begins to increase, and once again the electrons gain enough energy for ionization to strongly compete with excitation. The final two regions are analogous to the Cathode Dark Space and Negative Glow. In the

Anode Dark Space the luminosity decreases due to ionization; in the Anode Glow newly formed electrons, accelerated by the increasing electric field, again reach the excitation threshold.

Returning to the positive column region in Figure 1, we note a number of interesting features; the axial electric field, luminosity, electron number density, and current are all essentially constant. In addition, while the size of the other regions depends on the electron mean free path, the length of the positive column scales with the tube. As the tube grows longer, so does the positive column; if the tube is too short, the column may disappear altogether. The reason for this scaling comes from its purpose – it provides electrical continuity between the cathode and anode [6]. Because the positive column grows with tube length, it is often the largest of the glow discharge segments. These properties will be exploited later to simplify our model of the glow discharge.

Although Figure 1 and the resulting discussion considered only axial characteristics of the discharge tube, radial variations exist as well. In Figure 2, we see plots of experimentally determined radial space charge potentials within the cylindrically symmetric positive column. These potentials form as relatively light electrons speed toward the tube wall, leaving the heavier ions behind. This charge separation creates a potential and hence a radial component to the electric field. Because of the radial potential, any model which hopes to accurately describe the glow discharge needs to consider not only axial variations, but radial ones as well.

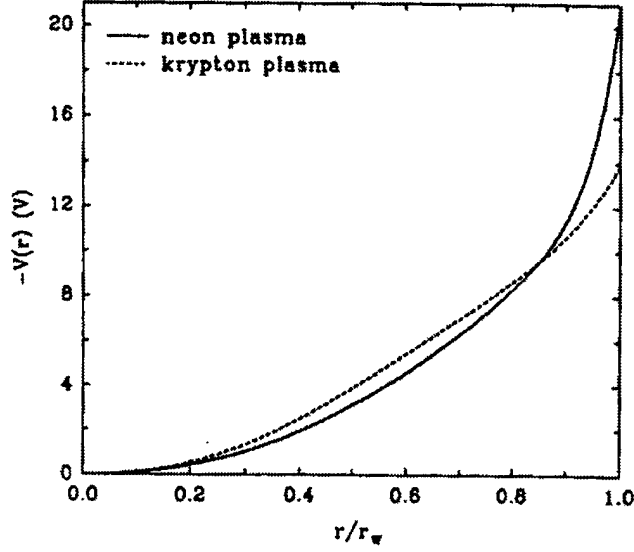


Figure 2 Experimentally determined radial potential ($-V[r]$ in Volts) as a function of normalized radius for neon and krypton at .62 and 4.8 Torr respectively [7].

Due to the sheer numbers of particles involved, electrons in the system are often treated statistically and characterized using a distribution function. The electron velocity distribution function (EVDF), labeled f , represents the number of particles found at a set of coordinates, e.g. $f[x, y, z, v_x, v_y, v_z, t]$. To find the total number of particles at a given spatial location the EVDF is integrated over velocity space, i.e. $\int_{-\infty}^{\infty} f[\vec{r}, \vec{v}] d\vec{v} = n_e[r]$.

By considering an electron distribution, we ignore the motions of individual particles, treating the plasma statistically. This approximation is justified for all but the most tenuous of gases, and it is certainly acceptable in our pressure range of interest, 0.1-10 Torr. Once the distribution function is known, we can derive all of the relevant macroscopic quantities using moments of the Boltzmann equation (see Appendix A). These quantities, such as the excitation collision rate (equation (44)), correspond directly to important measurable parameters like the luminosity.

Often the distribution function is transformed from velocity to energy coordinates, and then referred to as the electron energy distribution function (EEDF). Figure 3 shows examples of four different EEDFs. The first two, (a) and (b), result from approximate solutions of the CBE, under the assumption of constant collision frequency and constant collision cross-section respectively. The third and fourth represent more physically realistic distributions, for the case of a noble gas, (c), and a simple molecular gas, (d).

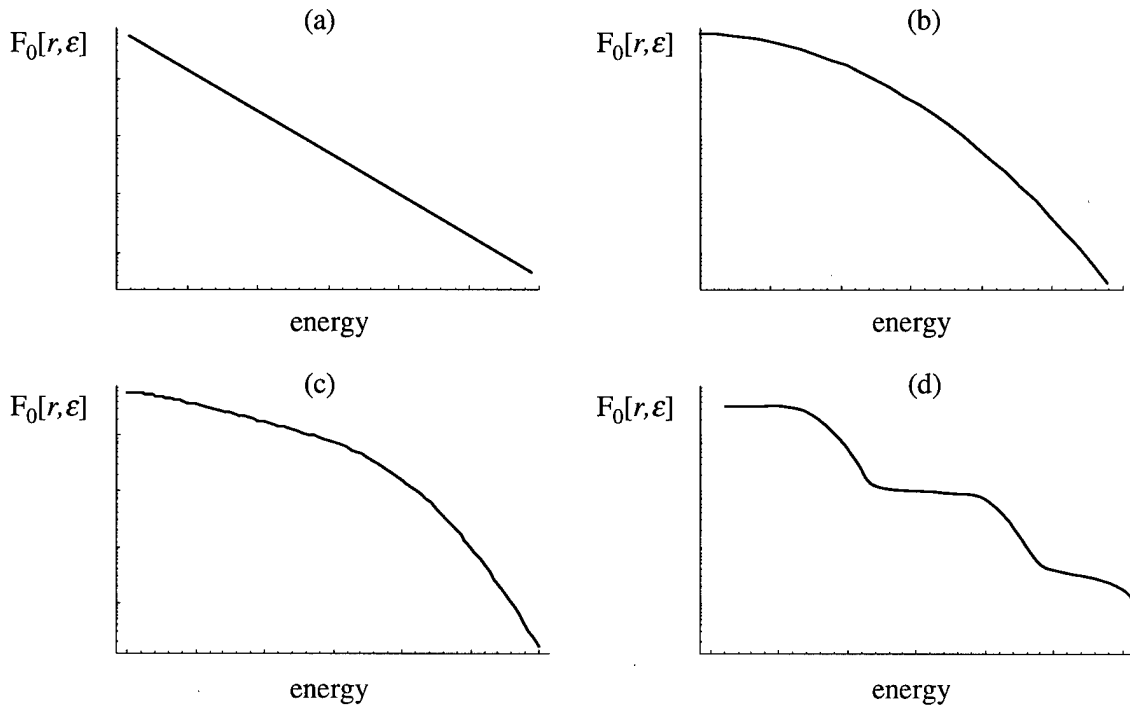


Figure 3 Four examples of the electron energy distribution function plotted on a log/linear scale: (a) Maxwellian, (b) Druyvesteyn, (c) typical Noble Gas, (d) typical Molecular gas.

2.1.2. Modeling the Glow Discharge

When trying to realistically model the electron kinetics of a glow discharge, we are forced to make a number of significant simplifications. The first simplification is to recognize that while most of the glow's segments are fixed in length for a given set of conditions, the positive column grows and shrinks with the tube length (section 2.1.1). If

the discharge tube is more than a few centimeters long, the positive column accounts for the majority of the discharge, and is thus considered the working section for most applications. To simplify our study, this treatment considers only the positive column³.

Having chosen to model only the positive column region of the glow discharge, we can then make use of its cylindrical symmetry and axial homogeneity (section 2.1.1). Accounting for these two properties, the required spatial dimension of the solution is reduced from three to one – the radial dimension.

Even with this simplification, modeling the dc positive column is extremely complicated; past authors have used a number of different techniques to tackle the problem. These techniques fall into three broad classes: Moment, Particle, and Kinetic methods. The moment methods include such classic treatments as Schottky's ambipolar diffusion theory and Tonks and Langmuir's free-fall theory. As the name suggests, moment methods use moments of the Boltzmann equation, treating the electrons as a fluid. These methods start with an assumed form for the EVDF, and use the resulting transport coefficients and collision frequencies to transform the problem into a set of fluid balance equations. Yet without experimental verification of the assumed distributions, the results are only qualitative. In spite of this, historically, most theoretical treatments of the positive column have relied on the moment method [8].

Particle methods, which include Monte Carlo and Particle-in-Cell, consider the forces and collisions acting on individual particles to predict their motions. Since it is currently impossible to account for the movement of over 10^{16} particles/cm³ (~ 1 Torr),

³ Cathode to anode models exist which attempt to account for the physics along the entire length of the

these techniques attempt to create a representative sample, and apply probability theory to extrapolate the total answer. Even so, particle methods require significant computational effort to obtain a solution, and even then are subject to sampling errors. Due to the computation time required, recent authors have suggested that techniques such as Monte Carlo are best suited to serve as benchmarks for other, faster methods [9].

The third class, the kinetic method, is the subject of this thesis. Kinetic methods solve directly for the EVDF using the collisional Boltzmann equation,

$$\frac{\partial f}{\partial t} + \vec{v} \cdot \vec{\nabla}_r f + \vec{a} \cdot \vec{\nabla}_v f = \left(\frac{\partial f}{\partial t} \right)_{collision} \quad (1)$$

where $f = f[\vec{r}, \vec{v}, t]$ is the EVDF.

The Boltzmann equation is in essence a continuity equation in both configuration and velocity space. The first term in equation (1) represents temporal changes to the EVDF, which for steady state solutions is zero. The second and third terms denote convection in configuration and velocity space respectively, where $\vec{\nabla}_r$ and $\vec{\nabla}_v$ are the corresponding gradient operators. The acceleration, \vec{a} , contains all of the forces acting on the electron, which in our study includes both a radial and axial electric field. The final term, $\left(\frac{\partial f}{\partial t} \right)_{collision}$, accounts for all of the collisions. It acts as both a source and a loss, depending on the type of collision and region of velocity space considered. A discussion of the various collisions included in this model is presented in section 3.1.2.

Because of the difficulty associated with solving equation (1) directly, early pioneers of the kinetic method looked to further simplify the problem. They did this by discharge tube, but this treatment considers only the positive column.

considering limiting forms for the CBE in the high and low-pressure range. These two limits correspond respectively to the local and nonlocal kinetic approximations. While the treatment in this thesis uses a strict kinetic solution, which is valid in both pressure regimes, we will gain significant insight by first reviewing the approximate solutions.

2.2. The Local Approximation

One of the first solutions using the kinetic method was published in 1946 by Holstein [10]. In this work, Holstein investigated the properties of a discharge in which he assumed the electric field to be everywhere homogeneous. Under these conditions, the spatial gradient of the distribution function must be zero, and the expansion of equation (1) results in an ordinary differential equation (ODE). The ODE is given below,

$$\frac{d}{d\epsilon} \left(\frac{\epsilon(e_o E_z)^2}{3NQ[\epsilon]} \frac{d}{d\epsilon} F[\epsilon] \right) + \frac{2m}{M_N} \frac{d}{d\epsilon} (\epsilon^2 NQ[\epsilon] F[\epsilon]) + S' = 0 \quad (2)$$

where N is the neutral number density, $Q[\epsilon]$ the total collision cross section, and S' accounts for inelastic collisions. $F[\epsilon]$ is the EEDF, normalized such that

$$\int_0^\infty F[\epsilon] \epsilon^{1/2} d\epsilon = 1.$$

If we consider only certain types of collisions, equation (2) can be solved analytically. Neglecting inelastic collisions and assuming a constant elastic collision frequency, the analytic result is the Maxwellian distribution shown in Figure 3a. If, on the other hand, elastic collisions are represented with a constant collisional cross section, the solution is a Druyvesteyn distribution given by,

$$F_{Dru}[\epsilon] = \frac{2}{\Gamma[3/4]} \left(\frac{3m}{M_N} \right)^{3/4} \left(\frac{NQ^{el}}{e_o E_z} \right)^{3/2} \exp \left[\frac{-3m(NQ^{el})^2 \epsilon^2}{M_N (e_o E_z)^2} \right] \quad (3)$$

where Q^{el} refers now to the elastic cross section only. The Druyvesteyn distribution is shown in Figure 3b. Although these analytic solutions exist, in practice equation (2) is solved numerically using a complete set of experimentally consistent elastic and inelastic cross-sections [11].

While the assumption of a homogeneous electric field greatly simplifies the CBE, it is rarely true in a physical discharge device. As discussed in section 2.1.1, we can treat the positive column as having a homogeneous *axial* electric field, but Figure 2 demonstrates that radial inhomogeneities do exist. However, under certain conditions, it is possible to neglect the effect of these radial variations, and justify the use of equation (2). If the pressure in the discharge is high enough, the electrons will undergo sufficient collisions to lose all of their energy (relax in energy space) prior to traveling an appreciable distance radially. Assuming the radial distance traveled is small enough, the electrons will not “see” any variation in the electric field. Under these conditions, the energy distribution of electrons is determined solely by the *local* electric field and equation (2) is justified. This assumption is called the Local Approximation.

In order for the local approximation to be accurate, the electron energy relaxation length must be much shorter than the characteristic length for field variations. One way to quantify this requirement is through the PR value, where P is the pressure in Torr, and R is the tube radius in centimeters⁴. Using a random walk analysis and the fact that an

⁴ A more appropriate measure would be NR where N is the number of molecules and R the radius, but I will follow the convention of Ingold [8] and use PR .

electron loses only a small fraction, $\frac{2m}{M_N}$, of its energy per elastic collision, the electron energy relaxation length L is given by

$$\langle L^2 \rangle = \frac{M_N}{2m} N^{-2} Q_{\text{momentum transfer}}^{-2} \quad (4)$$

where Q is the average momentum transfer cross-section in angstroms squared and N the neutral number density. Taking the characteristic distance for field variations to be the tube radius R , we can approximate the “ PR ” delimiter as

$$\begin{aligned} NR &\gg 60/T \sqrt{M_N/m} Q_{\text{momentum transfer}}^{-1} \\ PR &\gg 0.2 \sqrt{M_N/m} Q_{\text{momentum transfer}}^{-1} \end{aligned} \quad (5)$$

where T is 300K. Applying equation (5) to neon gas, the relaxation length requirement is met if $PR \gg 17$ Torr-cm. Given that lamps and electric discharge lasers operate at PR values on the order of one Torr-cm, this requirement is rarely satisfied in practice.

Further difficulties exist in applying the local approximation to realistic devices. In deriving equation (5) we chose the characteristic distance for field variations to be the tube radius. But as shown in Figure 2, the radial potential, and hence its derivative, the radial electric field, vary rapidly near the tube wall. These rapid changes invalidate the earlier approximation of the electrons not “seeing” field variations. We will find that even when the requirement of equation (5) is satisfied, the local approximation is never accurate near the tube wall.

2.3. The Nonlocal Approximation

When the PR value is much less than equation (5), the electrons are able to repeatedly traverse the discharge tube before relaxing in energy space. For this low-

pressure regime, the electrons sample the entire tube and carry with them a “memory” of the electric field variations throughout. Because of this, their energy distribution is no longer a function of the *local* electric field, rather it is a function of the *average* electric field and its variation. In this case a new, approximate solution is available – the Nonlocal Approximation. Bernstein and Holstein were the first to explore this low-pressure limit, publishing a paper in 1954 [12].

Taking into account the radial potential shown in Figure 2, the expansion of equation (1) results in a partial differential equation (PDE) in two dimensions, energy and radius. Much like the local case, the nonlocal approximation simplifies the problem to an ODE in energy only. In this instance, however, the transformation is achieved by averaging over the spatial derivatives, rather than neglecting them [6]. In order to justify the radial averages, the electron energy relaxation length must greatly exceed the tube radius. In other words, the pressure or *PR* of the system must be low, which is the opposite of the condition in equation (5).

After averaging, the CBE becomes

$$\begin{aligned} \frac{d}{d\varepsilon} \left(\frac{(e_o E_z)^2}{3N} \frac{d}{d\varepsilon} (p[\varepsilon] F[\varepsilon]) \right) + \frac{2mN}{M_N} \frac{d}{d\varepsilon} (q[\varepsilon] F[\varepsilon]) + S'' = 0 \quad (6) \\ p[\varepsilon] = \int_0^{r_o} \frac{(\varepsilon - \phi[r])}{Q[\varepsilon - \phi[r]]} r dr \\ q[\varepsilon] = \int_0^{r_o} (\varepsilon - \phi[r])^2 Q[\varepsilon - \phi[r]] r dr \end{aligned}$$

where Q is again the total collision cross section, but S'' is now an averaged inelastic collision term. The two additional terms, $p[\varepsilon]$ and $q[\varepsilon]$, calculate the necessary averages over the dimensions of the tube, and involve the electron motive, $\phi[r] = -V[r]$. With the addition of a radial potential, the kinetic energy, u , depends not only on ε , but r as well.

Equation (6) looks very similar to (2) for the local approximation, and as in that case analytic solutions exist under certain conditions. Assuming no inelastic collisions and a constant elastic cross section we arrive at a modified Druyvesteyn distribution,

$$F_{\substack{Nonlocal \\ Dru}}[\epsilon] = \frac{2}{\Gamma[3/4]} \left(\frac{2m}{M_N} \right)^{3/4} \left(\frac{NQ^{el}}{e_o E_z} \right)^{3/2} \exp \left[\frac{-2m(NQ^{el})^2 \epsilon^2}{M_N (e_o E_z)^2} \right] \quad (7)$$

where we have assumed a quadratic potential (the solution is slightly different depending on the form of the potential). Bernstein and Holstein [12] first derived equation (7) in planar geometry, but we have converted it to cylindrical coordinates for this treatment.

While the local and nonlocal approximations adequately describe discharge kinetics in their respective pressure regimes, the regimes are not well defined. In addition, there exists a significant gap between the two approximations where neither is very accurate. Most physical glow discharge devices live in this gap and are thus, at present, poorly described. Only through a strict solution of the complete, expanded CBE can we accurately model the middle pressure regime. The remainder of this thesis investigates that strict kinetic solution.

III. Methodology of the Strict Kinetic Solution

This chapter develops the theoretical equations used to model the positive column region of a dc glow discharge, then presents the numerical techniques used to solve the resulting partial differential equation. The development in section 3.1.1 is necessarily condensed, and focuses on understanding the assumptions made and resulting terms in the equations. A more thorough derivation is provided in Appendix B.

3.1. Theoretical Development of Solution Equations

3.1.1. Expansion of the Collisional Boltzmann Equation

Using the strict kinetic method, we solve for the distribution of electrons within the positive column as a function of position and velocity (or energy). As stated in section 2.1.2, the starting point for the derivation is the collisional Boltzmann equation,

$$\frac{\partial f}{\partial t} + \vec{v} \cdot \vec{\nabla}_r f + \vec{a} \cdot \vec{\nabla}_v f = \left(\frac{\partial f}{\partial t} \right)_{\text{collision}} \quad (8)$$

where $f = f[\vec{r}, \vec{v}, t]$ is the electron velocity distribution function normalized to the electron density, i.e. $\int_{-\infty}^{\infty} f[\vec{r}, \vec{v}] d\vec{v} = n_e[\vec{r}]$.

Reiterating the discussion of section 2.1.2, the Boltzmann equation is an electron continuity equation in both configuration and velocity space. In our steady-state treatment, the first term, representing temporal changes to the EVDF, is zero. The remaining terms balance the divergence of the electron flux with gains and losses due to collisions. A complete discussion of the various collisions included in the model is presented in section 3.1.2.

By writing a Boltzmann equation only for the electrons and not the other “secondary” constituents (e.g. ground state neutrals, ions, etc.), we are essentially assuming a form for their distributions. In this treatment we treat the secondary species as being uniformly distributed spatially, and as having negligible temperature. This is a reasonable assumption given the large mass ratio between the secondary constituents and electrons, and considering the relatively low neutral gas temperatures observed within the plasma. Making it allows us to de-couple an otherwise complicated system. We are left with the single Boltzmann equation, albeit in six dimensions, describing an EVDF that contains all of the phenomenon of interest in the system [13].

Solving the Boltzmann equation in six dimensions is a daunting task, so further assumptions are made to simplify the problem. The next widely used assumption is to assert that for the conditions of interest the EVDF is nearly isotropic. This allows us to expand the EVDF in spherical harmonics in velocity space, keeping only the first two terms.

$$f[\vec{r}, \vec{v}] = \sum_l P_l(\cos[\theta]) f_l(\vec{r}, v) \\ \equiv f_0[\vec{r}, v] + \frac{\vec{v} \cdot \vec{f}_1[\vec{r}, v]}{|\vec{v}|} \quad (9)$$

Here f_0 is the isotropic part of the EVDF, while $\frac{\vec{v} \cdot \vec{f}_1}{v}$ refers to the anisotropic part.

Notice that \vec{f}_1 is a vector, which can be resolved into radial and axial components, f_r and f_z respectively. Further simplifications are made by moving from $\vec{v} \Rightarrow v$, incorporating the vector information directly into the equations. By recognizing the cylindrical symmetry and axial homogeneity of the positive column (section 2.1.1) we finally reduce the problem from six dimensions down to two, one radial and one speed.

The previous two-term expansion is valid if: the energy gained from the electric field between collisions is small, and the total number of elastic collisions is significantly greater than the inelastic ones. These conditions ensure the electrons are well distributed in velocity space, i.e. isotropic, and for the conditions of interest are generally considered valid [14, pg 2].

As derived in Appendix B, the solution continues by substituting (9) into (8), expanding the $\vec{\nabla}$ operators, and keeping just the zeroth and first order terms. We also consider the source/loss terms in the collision integral, adding the contributions from elastic and inelastic collisions, as well as electron production arising from collisions between excited state neutrals.

With further manipulations, the final result is a single elliptic PDE. In this transformed state, the solution is a function of radial position and total energy; in other words, \tilde{f}_0 is now the electron energy distribution function. The CBE for the strict kinetic method becomes

$$\frac{1}{r} \frac{\partial}{\partial r} \left(\frac{ru}{3K[r, \epsilon]} \frac{\partial}{\partial r} \tilde{f}_0 \right) + \frac{\partial}{\partial \epsilon} \left(\frac{u(e_o E_z)^2}{3K[r, \epsilon]} \frac{\partial}{\partial \epsilon} \tilde{f}_0 \right) + \frac{\partial}{\partial \epsilon} (G[r, \epsilon] \tilde{f}_0) - uH[r, \epsilon] \tilde{f}_0 + \tilde{S}_0[r, \epsilon, \tilde{f}_0] = 0 \quad (10)$$

where

$$G[r, \epsilon] \equiv \sum_k 2 \frac{m}{M_k} u^2 N_k Q_k^{el}[u] \quad (11)$$

$$H[r, \epsilon] \equiv \sum_k \sum_l N_k Q_{kl}^{ex}[u] + \sum_k \sum_l N_k Q_{kl}^{de}[u] + \sum_k N_k Q_k^{io}[u] \quad (12)$$

$$K[r, \epsilon] \equiv \sum_k N_k Q_k^{el}[u] + H[r, \epsilon] \quad (13)$$

$$S_0[r, u, f_0] \equiv \sum_k \sum_l u'_{kl} N_k Q_{kl}^{inelas}[u'_{kl}] f_0[r, u'_{kl}] \quad (14)$$

These term definitions follow the formalism of Uhrlandt and Winkler [7, pg 520].

Specific parameters include: E_z - the axial electric field; N_k - the number density, where k refers not only to different neutral species, but also to different excited states of the same species; m - mass of the electron; M_k - mass of the neutral species k ; and $Q_{kl}^{process}[u]$ - the collisional cross section, which depends not only on the process involved, but the kinetic energy and collision partners.

Interpreting equations (11)-(17), $G[r, \epsilon]$ is the scaled elastic momentum transfer term. $H[r, \epsilon]$ sums the three inelastic collisions (excitation, de-excitation, and ionization), becoming the total inelastic term, while $K[r, \epsilon]$ includes both elastic and inelastic collisions, giving the total momentum transfer term. $\tilde{S}_0[r, \epsilon, \tilde{f}_0]$ is a source term, adding electrons at energy u based on inelastic collisions taking place at other energies u' .

Upon closer inspection, we recognize that (10), like (8), is a continuity equation.

The first term, $\frac{1}{r} \frac{\partial}{\partial r} \left(\frac{ru}{3K[r, \epsilon]} \frac{\partial}{\partial r} \tilde{f}_0 \right)$, represents the divergence of the radial flux; as u increases, the flux increases, while as $K[r, \epsilon]$ (the total collision term) increases, the radial flux decreases. The second term, $\frac{\partial}{\partial \epsilon} \left(\frac{u(e_0 E_z)^2}{3K[r, \epsilon]} \frac{\partial}{\partial \epsilon} \tilde{f}_0 \right)$, denotes the divergence in energy space of an electric field driven flux; again this flux tends to increase as u increases, yet diminishes as $K[r, \epsilon]$ increases. The next term, $\frac{\partial}{\partial \epsilon} (G[r, \epsilon] \tilde{f}_0)$, is also the divergence of an energy flux, but this time due to elastic collisions. Finally, the last two terms are the losses and sources due to inelastic collisions; $-uH[r, \epsilon] \tilde{f}_0$ accounts for the losses at a

given r and ε that occur due to the various inelastic collisions. Corresponding gains from other energies appear in $\tilde{S}_0[r, \varepsilon, \tilde{f}_0]$.

In the course of deriving equation (10), the following relationships for the components of \vec{f}_1 arise (see Appendix B):

$$\tilde{f}_r[r, \varepsilon] = -\frac{1}{K[r, \varepsilon]} \frac{\partial}{\partial r} \tilde{f}_0[r, \varepsilon] \quad (15)$$

$$\tilde{f}_z[r, \varepsilon] = \frac{e_0 E_z}{K[r, \varepsilon]} \frac{\partial}{\partial \varepsilon} \tilde{f}_0[r, \varepsilon] \quad (16)$$

Equations (15) and (16) are used initially to formulate boundary conditions, and after solving the problem, to calculate macroscopic quantities of interest such as the particle and energy currents, radial and axial heating, and local particle and energy balances (see Appendix A).

Although the development of the CBE is complete, we have not yet specified exactly which collisions will be considered. In addition, the form for \tilde{S}_0 is still general. The next section addresses these issues.

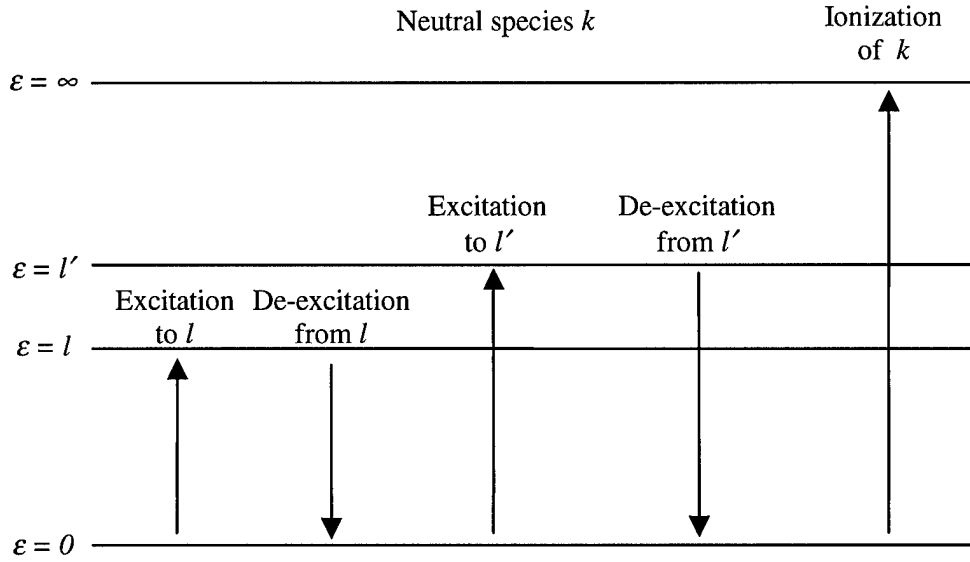


Figure 4 Energy level diagram depicting three types of inelastic electron collisions involving neutral species k and excited states l and l' .

3.1.2. Discussion of Collision Terms

Careful consideration of the relevant collision mechanisms is required to achieve a robust and flexible simulation, yet it is not necessary to include every possible type of collision in order to create a quantitatively accurate model of the system. Many of the collisions, such as electron/electron, rarely occur in the weakly ionized gases considered and therefore contribute little to the overall electron distribution. By disregarding negligible terms, the model remains accurate and relatively simple to implement.

Our treatment considers three classes of inelastic collisions: excitation, de-excitation, and ionization. We ignore volumetric recombination, choosing instead to assume that all recombination occurs at the wall as part of the wall loss boundary condition. This is a reasonable assumption for the low electron/ion densities considered as well as the relatively high electron temperature that results. In the case of elastic collisions, we include only electron/neutral and disregard electron/ion and

electron/electron collisions. This again limits the treatment to weakly ionized plasmas in which these types of collisions are negligible.

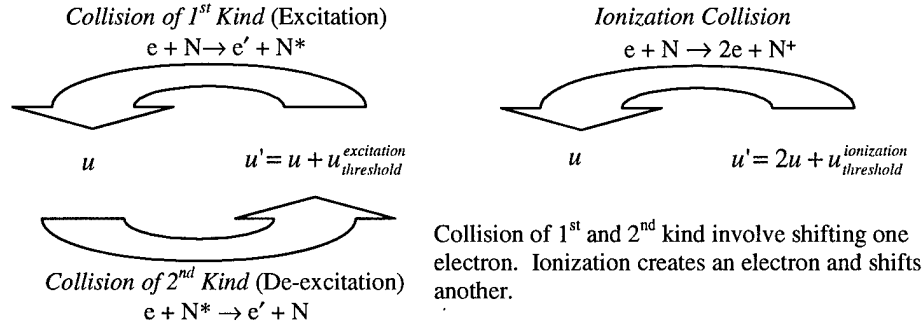


Figure 5 Electron scattering in three types of inelastic electron collisions.

The inelastic collisions considered in this model are represented in Figure 4 and Figure 5. Figure 4 illustrates the effect inelastic collisions have on the neutral species' internal energy levels. The complementary view in Figure 5 shows the effect of the same collisions on the kinetic energy of the electrons.

Excitation, or a collision of the first kind, inelastically scatters energetic electrons to lower energies, while promoting the colliding atom or molecule to a higher internal energy state. The electron's energy loss is equal to the excitation threshold of the neutral species. Because the plasma in this treatment is weakly ionized, excitation of ions is neglected. The density of excited state neutrals is also relatively small; thus any further excitation to higher electronic levels is also neglected.

The reverse process is de-excitation, a collision of the second kind, or a super-elastic collision. In this case, collisions occur between electrons and excited state neutrals, scattering the electrons to higher energies as the excitation energy of the neutral is transferred to kinetic energy in the electron. Once again the ion density is considered too small for excited-state ion/electron collisions to contribute to the solution.

In the case of ionizing collisions, we consider two types: between energetic electrons and ground state neutrals (Figure 4 and Figure 5), and between excited state neutrals (Penning ionization). As in the case of excitation, collisions between electrons and excited state neutrals (step-wise ionization) are disregarded.

The Penning ionization term is very important, from both a physical and computational standpoint. Consider the homogenous nature of equation (10), where every term depends on f_0 ; this means there are an infinite number of proportional solutions. In contrast, the Penning term depends only on the number density of excited state neutrals and the rate coefficient of electron production. Introduction of this term adds an inhomogeneity to the equation set, and resolves the solution. An inhomogeneous term can also arise through the introduction of certain boundary conditions, but not all boundary conditions produce this effect. It is therefore important to include the Penning ionization in order to obtain an absolute solution.

Returning to equation (10), the expression for S_0 is now expanded to show the contribution of each inelastic collision:

$$\begin{aligned}
 S_0[r, u, f_0] = & \sum_k \sum_{k^*} \sqrt{\frac{m}{2}} N_k N_{k^*} z_{kk^*} \delta[u^{Penning}] \\
 & + \sum_k \sum_l (u + u_{kl}^{ex}) N_k Q_{kl}^{ex} [u + u_{kl}^{ex}] f_0[r, u + u_{kl}^{ex}] \\
 & + \sum_k 4 (2u + u_k^{io}) N_k Q_k^{io} [2u + u_k^{io}] f_0[r, 2u + u_k^{io}] \\
 & + \sum_k \sum_l (u - u_{kl}^{de}) N_k Q_{kl}^{de} [u - u_{kl}^{de}] f_0[r, u - u_{kl}^{de}]
 \end{aligned} \tag{17}$$

Ignoring for a moment the Penning term, the other three are strikingly similar, combining a collisional interaction energy, neutral number density, cross section, and f_0 . The major difference between them is the interaction energy. This energy is the amount required for

the scattered electron to end up with kinetic energy u . For example, under excitation, the electron collides with a neutral, transferring energy equal to the excitation threshold (see Figure 4 and Figure 5). Therefore, for the electron to end up with kinetic energy u after the collision, it must have energy $u + u^{excitation}$ before the collision. The rationale is reversed for de-excitation. In the special case of ionization a new electron is formed, thus the interaction energy must be sufficient to overcome the ionization threshold and provide kinetic energy u to both electrons. By giving both electrons kinetic energy u , we have assumed that they equally share the excess energy.

Unlike excitation and de-excitation, the ionization term contains a prefactor of 4. This 4 is actually comprised of two parts: a factor of two to account for the newly released electron and a second factor of two that relates to the energy bin spacing. Consider the case of excitation, in that collision the scattered electron maps directly from one energy bin ($u + u^{excitation}$) to another (u). In ionization, however, the electron starts in an energy bin ($2u + u^{ionization}$) that is twice as wide as the destination bin (u). The second factor of two accounts for this difference in bin widths.

Returning to the case of Penning ionization, the number of electrons produced at energy u is a function of the number density of excited state neutrals and rate coefficient of electron production, z_{kk^*} . The delta function, $\delta[u^{Penning}]$, represents the assumption that all Penning electrons are produced at a single kinetic energy⁵, $u^{Penning}$. When the excited state neutrals collide, they relax to their ground states; the released energy frees

⁵ Some authors [7] choose to spread the Penning electrons out across a range of energies, but that is not done in this model.

an electron, with any remaining energy going into electron kinetic energy. Thus $u^{Penning}$ is equal to the sum of excitation thresholds of the colliding neutrals, minus the ionization threshold of the gas species.

3.1.3. Boundary Conditions to the Solution Equation

Before attempting a numerical solution to (10), the only remaining task is to specify boundary conditions to the solution area detailed in Figure 6. The four boundaries correspond to $r = 0$, $r = R_{\text{wall}}$, ϵ_{max} , and $u = 0$, since the kinetic energy of an electron can not be negative as the total energy goes to zero.

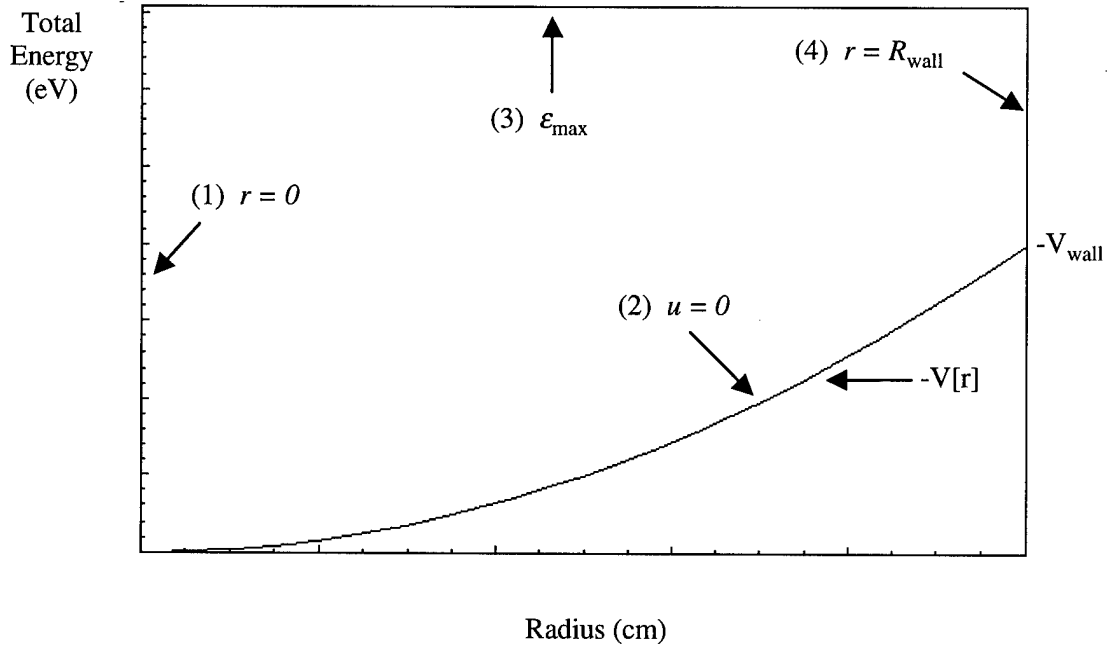


Figure 6 Diagram of typical solution area including the four boundaries. Boundaries (2)-(4) are determined at run-time by the input conditions.

Two of the boundaries are relatively straightforward. First, for the cylindrical systems usually associated with the positive column, the radial anisotropy, f_r , must be zero at $r = 0$ in order to remain symmetric around the axis.

$$\tilde{f}_r[r, \epsilon] = \left(-\frac{1}{K[r, \epsilon]} \frac{\partial}{\partial r} \tilde{f}_0[r, \epsilon] \right) \bigg|_{r=0} = 0 \quad (18)$$

For the $u = 0$ boundary we expand (10) and take the limit as $u \rightarrow 0$ to obtain the second condition. This leads to

$$\left[(e_0 E_z)^2 \frac{\partial}{\partial \epsilon} - e_0 E_r[r] \frac{\partial}{\partial r} \right] \tilde{f}_0[r, \epsilon] \bigg|_{\epsilon = -e_0 V[r]} = 0 \quad (19)$$

The third boundary is not as straightforward. We require the EEDF to go to zero as $\epsilon \rightarrow \infty$, and this is in fact the boundary condition chosen by Uhrlandt and Winkler [7, pg 522]. Unfortunately, the numerical solution grid must end at some finite (preferably small) upper limit, and in that case the EEDF is not zero. We ran simulations of this boundary condition using a simple model that had an analytic answer. These simulations demonstrated that forcing the EEDF to zero prematurely introduced significant errors. The condition $\tilde{f}_0[r, \epsilon_{\max}] = 0$ is not valid unless the model is run to extremely high energies, but doing so exponentially increases the computer memory requirements and processing time. These same simulations lead to the resolution.

The analytic simulations showed that while setting the last energy bin to zero introduced significant errors, setting it to a fraction of the previous bin did not. Choosing the fraction amounts to specifying the slope of the EEDF at the highest energies [15, pg 282], and allows us to write $\tilde{f}_0[j_{\max}] = A \tilde{f}_0[j_{\max} - 1]$ where j refers to the energy index and A the fraction. Early versions of the model considered only elastic collisions with a

constant collisional cross section and no radial potential. Under these assumptions, (10) has an analytic solution, the Druyvesteyn distribution (section 2.2). This analytic result initially provided an excellent slope for the top boundary condition. However, once we included inelastic collisions into the model, the distribution became distorted enough from a Druyvesteyn to require a new functional form.

In order to successfully utilize the fraction A as an upper boundary condition, we needed an analytic function that reflected the contribution from inelastic collisions. At the highest energies, equation (10) takes on a limiting form in which the field driven flux toward higher energy is balanced by inelastic collisional losses. This equation can be solved approximately, providing an excellent choice for A . The derivation is found in Appendix C. With it, the third boundary condition becomes,

$$\begin{aligned}\tilde{f}_0[r, j_{\max}] &= A \tilde{f}_0[r, j_{\max} - 1] \\ A &= \exp[-\beta(u_{j_{\max}} - u_{j_{\max}-1})] \\ \beta &= \sqrt{\frac{3}{(e_o E)^2} K[r, \epsilon_{\max}] H[r, \epsilon_{\max}]}\end{aligned}\tag{20}$$

It is important to note that when implemented as written in (20), the boundary condition broke down near the wall. As r approaches R_{wall} , the kinetic energy u at ϵ_{\max} decreases. This constriction in energy space violates the earlier assumption of field driven flux balancing collisional losses. To overcome the problem, we used $u_{\max}[r=0]$ instead of $u_{\max}[r]$ when calculating both β and A . Another possible fix would be to find a new limiting form for the distribution that holds true near the wall. But this would also require merging the two boundary conditions at an intermediate r . As it stands, the

current method works well for the parameters of interest, and is superior to assuming

$$\tilde{f}_0[r, \epsilon_{\max}] = 0.$$

The last boundary condition at $r = R_{\text{wall}}$ is also difficult. Electrons with sufficient total energy may overcome the radial potential ($\epsilon \geq -e_0 V[r_{\text{wall}}]$) and be “absorbed” at the wall and hence lost to the system. Thus, at the wall, we need to include some form of loss mechanism; this loss will also balance the gains from ionization to produce the steady state. Again, initially following the paper of Uhrlandt and Winkler [7], we set the radial anisotropy equal to a proscribed loss function at the wall.

$$\tilde{f}_r[r_{\text{wall}}, \epsilon] = -\frac{1}{K[r_{\text{wall}}, \epsilon]} \frac{\partial}{\partial r} (\tilde{f}_0[r_{\text{wall}}, \epsilon]) = A \exp[-a u^2[r_{\text{wall}}, \epsilon]] \quad (21)$$

where the parameters a and A are available to adjust the total amount of loss (see section 4.4).

Uhrlandt and Winkler experimented with a number of different wall loss functions, most variations of the exponential form in (21) [16]. They came to the conclusion that except for the region very near to the wall, the solution to the EEDF yields essentially the same results independent of the loss function, provided that the integrated strength is the same [7, pg 524].

The Uhrlandt formalism is helpful because it provides inhomogeneous terms to resolve our solution, lessening the reliance on Penning ionization (see section 3.1.2). However the loss function form is only loosely physically based. The search for a more realistic wall loss mechanism led to recent work by Alves, et al. [17] in which they presented a more physically based boundary condition called the wall loss cone (see

Figure 7). Their derivation is, in turn, an extension of the previous work by both Busch and Kortshagen [15] and Tsendin and Golubovskii [18].

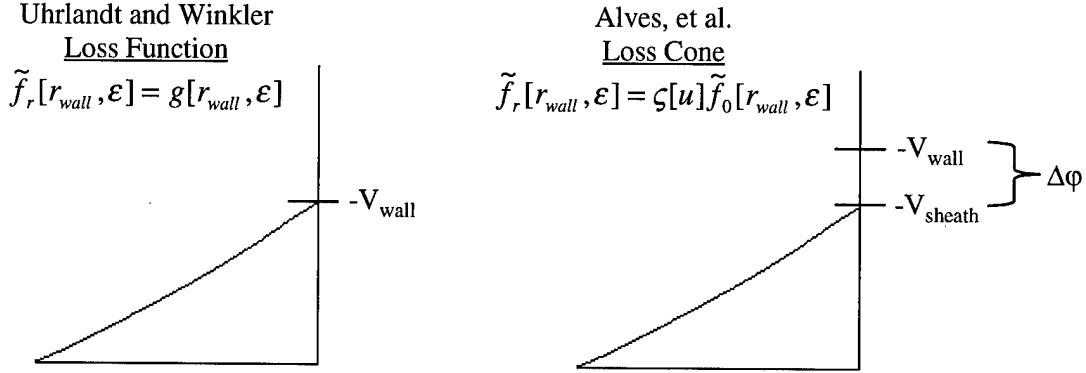


Figure 7 Comparison of the two types of wall loss boundary conditions.

Using the loss cone formalism, electrons must have enough kinetic energy *perpendicular* to the wall to surmount the wall potential. An additional parameter, the wall loss coefficient, permits only a fraction of the penetrating electrons to be lost. Unlike the previous wall loss development by Uhrlandt and Winkler, this formalism includes a region known as the plasma sheath, illustrated in Figure 7, which is found at the tube wall. The plasma sheath is assumed to be infinitely thin, and its main property of interest is the drop in potential that occurs across it. In the work by Alves, the sheath potential is taken to add an additional -4 to -8 eV to the wall potential [17, pg 899].

We wanted to consider both types of wall loss conditions in this treatment and therefore attempted to integrate both into the code. To do so, we chose to ignore the addition of the sheath potential, $\Delta\phi$, at the wall. Since our treatment can accept any arbitrary radial potential (section 3.2.1), we are always able to add an effective sheath

potential by modifying the input near the wall. This allows us to mimic the conditions considered by Alves, while including the Uhrlandt formalism as well.

Taking $\Delta\varphi = 0$, the modified loss cone boundary condition is,

$$\tilde{f}_r[r_{wall}, \epsilon] = -\frac{1}{K[r_{wall}, \epsilon]} \frac{\partial}{\partial r} (\tilde{f}_0[r_{wall}, \epsilon]) = \frac{3}{2} \frac{(1-\chi)}{(1+\chi)} \tilde{f}_0[r_{wall}, \epsilon] \quad (22)$$

where χ is the reflection coefficient, which runs from 0 to 1. Like the parameters a and A in (21), χ adjusts the total amount of loss occurring at the wall

Unlike the Uhrlandt formalism, the loss cone does not provide an inhomogeneous term for our solution set. This leaves only the Penning term to resolve the system. But in some cases, the contribution from Penning ionization is too small to accurately drive the system, resulting in an unstable solution. When this happens we choose to accept the homogeneous equations, and resolve the system by assigning the EEDF a value at a particular point in the system, e.g. set $\tilde{f}_0[r_{special}, \epsilon_{special}] = 1$. This allows us to solve the homogenous system rather than trying to force a suspect inhomogeneous solution.

With the equations developed, and the boundary conditions formed, we are ready to find a numerical solution to the elliptic differential equation.

3.2. Numerical Method of Solution

The numerical method used to solve (10) is clearly described in numerical analysis textbooks such as Burden and Faires [19]. We start by forming a grid over the solution space. This grid specifies all of the solution points within the space, as well as the boundary points. Next, the CBE and boundary conditions are discretized. This allows us to form an equation for each solution point involving its neighbors. The

complete set of equations corresponds to a linear system of the form $\mathbf{A} \mathbf{x} = \mathbf{b}$, which is solved for $\mathbf{x}(\tilde{f}_0)$ using Gaussian Elimination.

While the brief outline above points to the simplicity of the numerical method, a number of challenges arise during implementation that are presented in the following sections. The first is how to form a grid over the solution space (shown in Figure 8). The technique used to do this is covered in section 3.2.1. In forming the grid, we use unequal spacing in both the radial and energy directions. This unequal spacing requires a more complicated set of differencing equations than those used for equal grid spacing. Section 3.2.2 details this. Finally, the linear system depends on a matrix \mathbf{A} , which is sparse banded. While simple Gaussian Elimination can be used to solve it, a more sophisticated technique discussed in section 3.2.3 is employed which speeds the solution and reduces memory requirements.

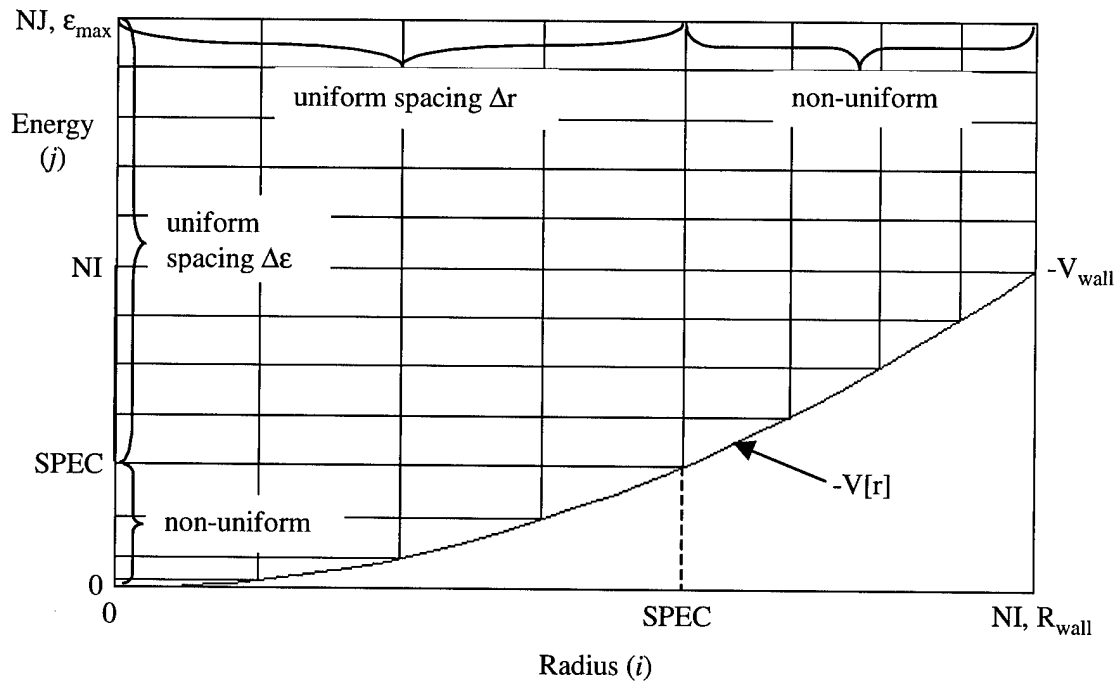


Figure 8 Diagram of basic parameters used in forming the solution grid.

3.2.1. Forming the Solution Grid

The first step in the numerical solution is to create a grid overlying the solution space. However, in our case, the shape of the solution space depends on the problem considered. Figure 6 shows that the lower boundary ($u = 0$) depends on the radial potential ($-V[r]$), which in turn depends on the specific parameters of the discharge; so the gridding technique must be able to handle a “general” input potential.

Although using a uniform mesh is desirable, a number of problems immediately arise. First, the grid points do not necessarily intersect the $u = 0$ boundary. This would force us to interpolate the boundary condition and solution in this region. Second, the shape of the potential dictates that some regions require a finer grid than others do. This is especially true near the wall, where the potential can change rapidly. These difficulties convince us to forgo uniform spacing and employ a non-equidistant mesh.

To create the grid, first consider Figure 8, which shows the relationship between the various grid parameters. In the diagram, NI and NJ refer to the maximum bin index in the radial and energy directions respectively. $SPEC$ is a special value chosen to optimize the density of grid lines; during implementation $SPEC$ is normally set to be $NI/2$. Using Figure 8 we can write equations which relate the various parameters.

$$SPEC \cdot \Delta r + r_{non-uniform} = R_{wall} \quad (23)$$

$$r_{non-uniform} = \sum_{i=SPEC+1}^{NI} (r_i - r_{i-1}) \quad (24)$$

$$(NI - SPEC)\Delta\epsilon + \epsilon_{non-uniform} = -V_{wall} \quad (25)$$

$$\begin{aligned} \epsilon_{non-uniform} &= \sum_{j=0}^{SPEC-1} (\epsilon_{j+1} - \epsilon_j) \\ &= -V[SPEC \cdot \Delta r] \end{aligned} \quad (26)$$

At this point the equation set is underdetermined. In order to resolve the system, we choose to enforce a relationship between the two uniformly spaced regions. We force the normalized distance between 0 and $SPEC$ on the radial axis and $SPEC$ and NI on the energy axis to be the same. This relationship produces equation (27), and with the use of (23)-(26) allows us to solve for $\Delta\epsilon$.

$$\frac{SPEC \cdot \Delta r}{R_{wall}} = \frac{(NI - SPEC) \cdot \Delta\epsilon}{-V_{wall}} \quad (27)$$

$$\Delta\epsilon = \frac{-V_{wall} + V\left[\frac{R_{wall}}{-V_{wall}}(NI - SPEC) \Delta\epsilon\right]}{NI - SPEC} \quad (28)$$

With these six equations we now have a method to generate the grid:

- a) Input the parameters NI , $SPEC$, R_{wall} , V_{wall} , ϵ_{max} . Input $-V[r]$ as a set of data points, this will also permit calculation of the inverse, $-V^{-1}[r]$.
- b) Calculate $\Delta\epsilon$ using the transcendental equation (28).
- c) Find Δr using (27) and $NJ = \frac{\epsilon_{max} + V_{max}}{\Delta\epsilon} + NI$
- d) Create part of the radius grid. From $i=1$ to $SPEC$, $radius[i] = radius[i-1] + \Delta r$
- e) Create the energy grid. From $j=1$ to $SPEC$, $energy[j] = -V[radius[j]]$. And for $j=SPEC+1$ to NJ , $energy[j] = energy[j-1] + \Delta\epsilon$.
- f) Finish the radius grid. From $r=SPEC+1$ to NI , $radius[i] = -V^{-1}[energy[i]]$.

After completing steps a) through f), the grid is formed.

As mentioned earlier, each intersection on the grid corresponds to either a solution point or boundary point. The distinction is that every solution point has a corresponding equation assigned to it, while the boundary points are used only to form the equations of their neighbors. In this treatment we decided to include three of the

boundaries in the solution space, reserving the top boundary, ϵ_{\max} , solely as a boundary condition.

Figure 9 shows the solution grid in i - j space; notice that unlike the radius-energy grid in Figure 8, the spacing is uniform. In addition, the $u = 0$ boundary is always a straight line, regardless of the input potential ($-V[r]$). For these reasons, it is often easier to think of the solution grid in i - j space rather than radius-energy.

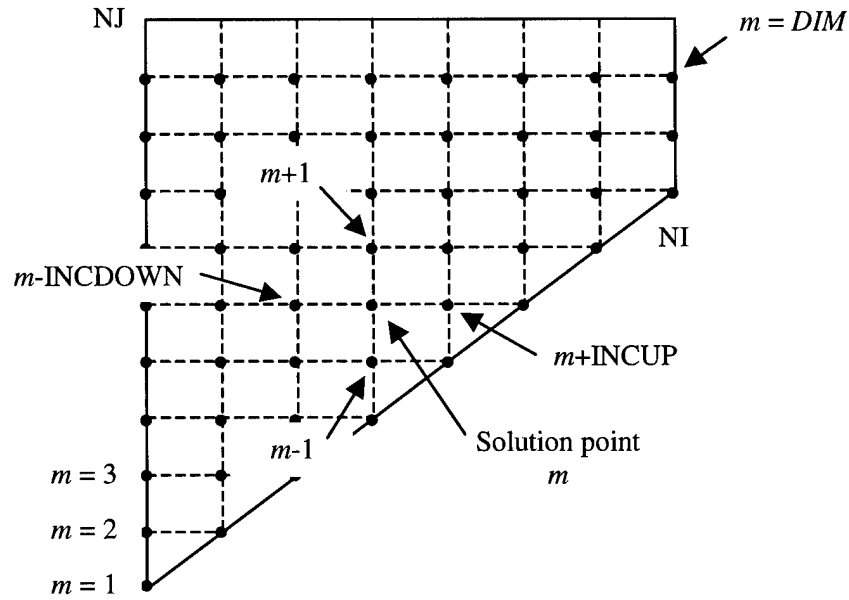


Figure 9 A schematic of the grid in i/j space. Solution points, m , are numbered sequentially from 1 to DIM .

The solution points are numbered sequentially starting at the origin, $m = 1$, and proceeding up the energy axis to the last bin, $NJ-1$. The count continues in the next radial bin, starting at $i = j$, and continuing to the last point when $i = NI$ and $j = NJ-1$. This last point corresponds to the total number of equations and solution points in the grid, and is referred to as DIM , the dimension of the solution. When we employ the finite differencing scheme (section 3.2.2) we will need to refer to the points surrounding every

solution point. In the energy (j) direction we can simply add or subtract one to reference the surrounding solution points. In the radial direction however, the enumeration is not that simple, and we must use counting variables *INCUP* and *INCDOWN*. There are also occasions where we must refer to points two radial bins away from a solution point; in those cases we use the variables *INC2UP* and *INC2DOWN*. With the help of Figure 9, we derive the following expressions for the variables in the counting scheme,

$$m = j - i + 1 + iNJ - \frac{i(i-1)}{2} \quad (29)$$

$$DIM = \frac{2NJ - NI + 2NI NJ - NI^2}{2} \quad (30)$$

$$INCUP = NJ - i - 1 \quad (31)$$

$$INCDOWN = NJ - i \quad (32)$$

$$INC2UP = 2NJ - 2i - 3 \quad (33)$$

$$INC2DOWN = 2NJ - 2i + 1 \quad (34)$$

Now that each solution point has a label, m , and we have a mechanism to reference the surrounding points, we are ready to transform the equations into a finite differencing form.

3.2.2. Finite Differencing on the Non-Uniform Grid

In order to write an equation for each solution point in the grid, equation (10) must be transformed from an analytic PDE into a differenced equation. In the case of uniform grid spacing this means using well known formulae such as the three point equation,

$$\left. \frac{\partial^2}{\partial r^2} f[r, \epsilon] \right|_{i,j} \cong \frac{f[r_{i+1}, \epsilon_j] - 2f[r_i, \epsilon_j] + f[r_{i-1}, \epsilon_j]}{h^2} \quad (35)$$

which approximates the second order derivative, $\frac{\partial^2}{\partial r^2} f[r_i, \epsilon_j]$, on a uniform grid with step-size h . Since the grid spacing in our treatment is not uniform, we require slightly more complicated versions of (35).

This analysis follows the example of Uhrlandt and Winkler [7, pg 528], employing a three point central-differencing scheme except at the boundaries, where we invoke either forward or backward differencing. The equations are derived using the Method of Undetermined Coefficients, outlined in most numerical analysis textbooks. The results are presented below, along with a number of step relations used to simplify the expressions.

$$\left. \frac{\partial}{\partial r} f[r, \epsilon] \right|_{i,j} \equiv h_{i,j} \equiv B_i (\alpha_i \cdot (f_{i+1,j} - f_{i,j}) - \beta (f_{i-1,j} - f_{i,j})) \quad (36)$$

$$\left. \frac{\partial}{\partial r} f[r, \epsilon] \right|_{i-1,j} \equiv h_{i-1,j} \equiv B_i (-\alpha_i \cdot (f_{i+1,j} - f_{i,j}) - (\beta_i + 2)(f_{i-1,j} - f_{i,j})) \quad (37)$$

$$\left. \frac{\partial}{\partial r} f[r, \epsilon] \right|_{i+1,j} \equiv h_{i+1,j} \equiv B_i ((2 + \alpha_i)(f_{i+1,j} - f_{i,j}) - \beta (f_{i-1,j} - f_{i,j})) \quad (38)$$

where h is introduced as a shorthand notation, and

$$\begin{aligned} B_i &= 1/(r_{i+1} - r_{i-1}) \\ \alpha_i &= (r_i - r_{i-1})/(r_{i+1} - r_i) \\ \beta_i &= 1/\alpha_i \end{aligned} \quad (39)$$

Similar expressions are also developed for $\frac{\partial}{\partial \epsilon} f[r, \epsilon]$ where B , α , and β become C , γ

and δ respectively. Equations (36)-(38) are used further to develop expressions for the second derivative. In the case of central differencing, this becomes

$$\frac{\partial}{\partial r} \left(P[r, \varepsilon] \frac{\partial \tilde{f}_0}{\partial r} \right)_{i,j} \equiv B_i (\alpha_i (P_{i+1,j} h_{i+1,j} - P_{i,j} h_{i,j}) - \beta_i (P_{i-1,j} h_{i-1,j} - P_{i,j} h_{i,j})) \quad (40)$$

where $P[r, \varepsilon]$ is an arbitrary function. Again, very similar expressions arise for the second derivative with respect to energy.

Using (40) and the corresponding equation for energy, we can transform (10) into finite differenced form. At the grid boundaries, care is taken to use either a forward or backward differencing equation such as (37) or (38), and to substitute in the appropriate boundary condition. The complete set of differenced equations is rather long, so it is presented in Appendix D.

Once the CBE is transformed, it can be evaluated at each solution point. Each solution point then has a corresponding equation, and we are ready to solve the resulting linear system.

3.2.3. Solving the Sparse Banded Matrix

Once every solution point in the grid has an equation associated with it, the entire problem is reduced to solving a linear system of equations of the form $\mathbf{A} \mathbf{x} = \mathbf{b}$. These systems are readily solved using Gaussian elimination, and many algorithms are available which implement this technique. However, simple Gaussian elimination is rather slow since the number of operations required is proportional to the cube of the number of matrix elements. Early test runs on a Pentium 166 took approximately one hour to solve a system with only 50 radial and 70 energy (50 X 70) bins. Our goal was to do “production” runs with approximately 300 X 500 bins, which, using equation (30), corresponds to an \mathbf{A} matrix with over 10^{10} elements. This would have severely taxed currently available super-computing resources.

$$\begin{array}{ccc}
\left(\begin{array}{cccccccc}
a_{11} & a_{12} & & & & & & \\
a_{21} & a_{22} & a_{23} & & & & & \\
a_{31} & a_{32} & a_{33} & a_{34} & & & & \\
& a_{42} & a_{43} & a_{44} & a_{45} & & & \\
& & a_{53} & a_{54} & a_{55} & a_{56} & & \\
& & & a_{64} & a_{65} & a_{66} & a_{67} & \\
& & & & a_{75} & a_{76} & a_{77} & a_{78} \\
& & & & & a_{86} & a_{87} & a_{88}
\end{array} \right) & \Rightarrow & \left(\begin{array}{cccccccc}
& a_{12} & a_{23} & a_{34} & a_{45} & a_{56} & a_{67} & a_{78} \\
a_{11} & a_{22} & a_{33} & a_{44} & a_{55} & a_{66} & a_{77} & a_{88} \\
a_{21} & a_{32} & a_{43} & a_{54} & a_{65} & a_{76} & a_{87} & \\
a_{31} & a_{42} & a_{53} & a_{64} & a_{75} & a_{86} & &
\end{array} \right) \\
\text{(a)} & & \text{(b)}
\end{array}$$

Figure 10 Sparse Banded Matrix in traditional storage (a) and reduced storage (b) as required by DGBSV routine. Zero elements are not shown.

But the **A** matrix is special. As with most numerical PDE solutions, the **A** matrix is sparsely populated along the main diagonal. This special form is called sparse banded (see Figure 10). We can take advantage of the abundance of zeros in the matrix to reduce both the program's memory requirements and time of execution.

The obvious way to decrease the memory requirement is to store only the non-zero bands of the matrix. This requires special algorithms to create, initialize, and access the matrix elements, which adds time to the overall process, but the reward is a dramatic reduction in the amount of memory required. In the case of a 300 X 500 grid, the number of matrix elements held in storage falls from 10^{10} to 10^8 using this technique.

Advance knowledge of the many zeros in the matrix can also dramatically reduce the number of operations needed to solve the system. The system is still solved by Gaussian elimination, except the algorithm is fine-tuned to speed the solution as much as possible. The specific algorithm used in this work is called "DGBSV" and comes from the LAPAC set of routines made available on the National Institute of Standards and Technology Internet site.

DGBSV requires the **A** matrix be transformed to a special form as shown in Figure 10. Under the transformation, each diagonal in **A** becomes a row in **A'**. The new

matrix has the same number of columns as \mathbf{A} , but the number of rows is reduced to $2NL+NU+1$. NL is the number of lower diagonals and NU the number of upper diagonals in \mathbf{A} . The first NL rows of \mathbf{A}' are filled with zeros initially, and used by the routine as a work space.

The DGBSV routine comes from a family of algorithms created to solve special matrices. It calls two other functions, DGBTRF and DGBTRS; the first computes the LU decomposition of \mathbf{A}' , while the second performs back substitution using \mathbf{b} to get the answer. This presents an opportunity to solve the problem quickly with multiple forcing vectors. Since the majority of the execution time is spent finding the LU decomposition of \mathbf{A}' , very little is added by calling DGBTRS multiple times. It also opens the window to efficiently implement a time dependent solution in the future.

The final size of \mathbf{A}' , and hence the time required to solve it, depends directly on the number of diagonals in \mathbf{A} , and the number of diagonals depends directly on the differencing scheme. In most cases, we use three point central differencing, which results in $2NJ-1$ diagonals in \mathbf{A} . However, as described in section 3.2.2, the lower boundary requires backward differencing in the radial direction. If the three point scheme is used, it increases the number of diagonals in \mathbf{A} to $3NJ-3$, which is a significant increase for large NJ . To circumvent this problem, we chose to employ only two point differencing on the lower boundary, keeping the number of diagonals in \mathbf{A} at $2NJ-1$. While the two point scheme is less accurate than three point, it is only used on the lower boundary, which constitutes a small fraction of the solution points, and testing showed that deviations between the two methods appear only in the 7th significant digit of the result.

Using the DGBSV algorithm instead of straight Gaussian elimination dramatically reduced the program's run time. The 50 X 70 bin test case, which previously took about an hour on a home PC, now finishes in less than one minute. The largest grids (300 X 500) are run at the Major Shared Resource Center on a SGI/Cray Origin 2000 computer. In those cases, the program requires 2 Gb of memory and takes about 30 minutes to finish when using only one CPU. The execution time of the solution scales approximately as the square of the number of solution points.

IV. Implementation of the Strict Kinetic Solution

In this chapter we step through four distinct phases of development and validation in the code. At each step we gain insight into the electron kinetics within the discharge, as well as establishing the capabilities and limitations of the model. The first phase treats the simple case of a homogeneous system, excluding inelastic collisions and assuming a constant elastic collision cross section. Under these restrictions, we have an analytic solution to validate the numerical solution; it is the Druyvesteyn distribution discussed earlier. Next, we add a non-trivial radial potential to the model, comparing the numerical results to an analogous analytic solution. In the third phase, we begin to add source and loss terms. While not physically representative collision terms, these point sources and losses demonstrate some of the capabilities of the model and elucidate behavior typical of the local and nonlocal regimes. Finally, we complete the development, adding the realistic collision terms as well as wall loss to the system.

4.1. Phase I: Radially Homogeneous System

This first version of the model neglects inelastic collisions and the influence of a radial electric field, and assumes a constant elastic cross section ($Q[u]=Q$). With these simplifications, (10) becomes

$$\frac{1}{r} \frac{\partial}{\partial r} \left(\frac{ru}{3K[r, \epsilon]} \frac{\partial}{\partial r} \tilde{f}_0 \right) + \frac{\partial}{\partial \epsilon} \left(\frac{u(e_o E_z)^2}{3K[r, \epsilon]} \frac{\partial}{\partial \epsilon} \tilde{f}_0 \right) + \frac{\partial}{\partial \epsilon} (G[r, \epsilon] \tilde{f}_0) = 0 \quad (41)$$

where u equals ϵ , since the radial potential is assumed zero. As there are no volumetric sources in the system and a steady state solution is sought, there can be no losses, and thus

the wall boundary condition is set to perfect reflection. In other words the flux of electrons at the wall is set to zero, $\tilde{f}_r|_{r=R_{wall}} = 0$.

Because the system is homogeneous by design, we know that the local approximation is satisfied (see section 2.2). As noted previously, assuming a constant elastic cross section and no inelastic collisions the CBE has an analytic solution; it is the Druyvesteyn distribution given in equation (3) and shown in Figure 3b. Recall that in the local approximation, the radial term $(\frac{1}{r} \frac{\partial}{\partial r} (\frac{ru}{3K[r, \epsilon]} \frac{\partial}{\partial r} \tilde{f}_0))$ is assumed negligible and dropped, whereas in the numerical model it is included but, if implemented correctly, still yields the local result.

We ran the model on a uniform grid with $NI = 10$ and $NJ = 100$, using only ten radial bins since the system was radially homogeneous. In order to compare the model output ($\tilde{f}_0[r, \epsilon]$) to the analytic result ($F[r, \epsilon]$), we normalized \tilde{f}_0 at each solution point, i.e. $F[r, \epsilon] = \tilde{f}_0[r, \epsilon]/n_e[r]$. Comparing the numerical model output to the analytic result at each solution point, we obtained relative errors between the two no greater than 1%.

The next step was to add a spatially varying radial potential.

4.2. Phase II: Include Radial Potential

Using the gridding technique presented in section 3.2.1, we added a general radial potential to the model. At this point, we still neglected all inelastic collisions; thus equation (41) remains valid. However, with the addition of the potential, the system is no longer radially homogeneous, and the local approximation does not necessarily hold. Although the system is no longer guaranteed to satisfy the local approximation, we can force it to this regime with a judicious choice of input parameters. Since we had already

validated Phase I against the local approximation, we chose here to compare to the nonlocal approximation.

As noted in section 2.3, we can, under certain assumptions, analytically solve (41) using the nonlocal approximation. With no inelastic collisions, a constant elastic cross section, and a quadratic form for the radial potential, we arrive at the modified Druyvesteyn distribution, equation (7). It is important to note that this 1-D derivation assumes that all electrons have a total energy less than $\phi[R_{\text{wall}}]$, which is effectively the same as assuming an infinite wall potential. Because our treatment is 2-D, it obviously includes a finite limit on ϕ at $r = R_{\text{wall}}$. To accommodate this difference, we reduced ϵ_{max} to $\phi[R_{\text{wall}}]$.

In the previous phase (section 4.1) the system was homogeneous, so we knew it satisfied the local approximation; but in this case we had to ensure the system was in the nonlocal regime. This meant setting the PR value such that the electron energy relaxation length was much greater than the tube radius, the opposite requirement of equation (4).

We ran the model for hypothetical gas at a pressure of 0.1 Torr and $r = 1\text{ cm}$ ($PR = 0.1$). As required, this PR is much less than the 3 Torr-cm established on the right-hand-side of equation (5). The addition of the radial potential forced us to employ the non-uniform grid of section 3.2.1, and we chose to set $NI = 100$ and $NJ = 105$ in an effort to approximate the energy mesh density of Phase I. Using these parameters, we again obtained relative errors between the analytic and numerical results of less than 1% throughout the volume.

Having added the radial potential into the system, we moved on to include volumetric sources and losses.

4.3. Phase III: Add Source and Loss Terms

With the addition of inelastic collisions, the model would be complete. But before addressing these complicated terms, we investigated how the model reacts to very simple losses and gains. As in the previous section, we continued to neglect inelastic collisions, assume a constant elastic collision cross section, and use a quadratic radial potential. Equation (41) is used to describe the system, along with a “total reflection” wall boundary condition.

We started by adding a simple point source to the volume at a given radius and energy. In this case the source term is an inhomogeneous addition to (41), e.g. $+10^{14}$, at one particular solution point, r', ϵ' . Since there are no losses at the boundaries, a volumetric loss is included to maintain a steady state. As with the source term, the loss is established at a single computational point, in this example r', ϵ'' . While the source term is inhomogeneous, the loss is proportional to the local population. Global particle conservation then fixes the population at the loss point such that $10^{14} = A \tilde{f}_0[r', \epsilon'']$, where A is the proscribed factor of proportionality.

Based on physical reasoning alone, we expect that at the source and loss points the EEDF will display “deviations” from the unperturbed Druyvesteyn form (Figure 3b page 9). Since electrons are being added at the source point (r', ϵ') , the distribution function there should be slightly higher than neighboring radial bins. Conversely, at the loss point (r', ϵ'') , where electrons are removed from the system, the distribution should show a deficit. We find in fact that this behavior is highly dependent on the pressure regime of the system.

Running the model at different pressures, we noticed a manifestation of local versus nonlocal behavior. In the local (high-pressure) case, the electron energy relaxation length is short; hence disturbances in the distribution function are confined to the radial location of the source/loss. In the nonlocal regime the opposite is true, and any disturbance in the distribution is propagated to all radii. Figure 11 illustrates these differences.

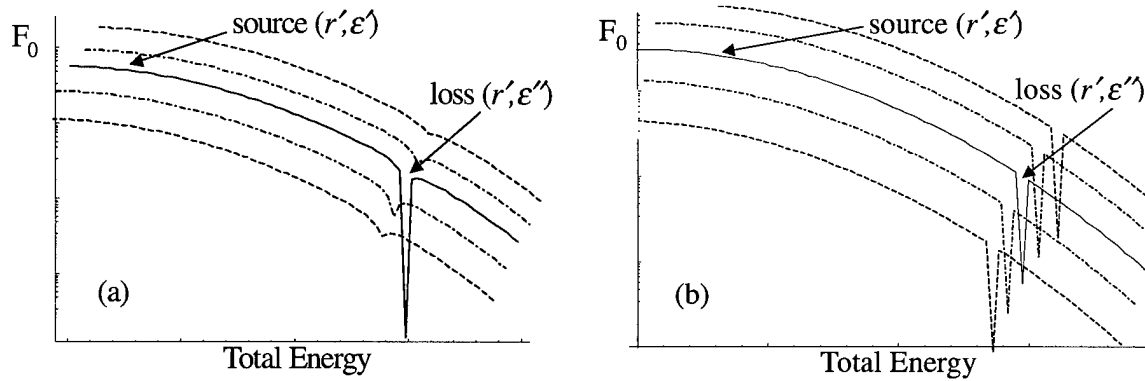


Figure 11 Log/linear plots of the EEDF versus total energy at five neighboring radial bins demonstrating the effect of a volumetric point gain/loss in the local (a) and nonlocal (b) regimes. The plots are vertically offset in order to distinguish differences between them.

In the figure above we see the results of the volumetric point gain/loss, and how its effect is propagated in radius. In both cases the solid line identifies the distribution at r' , the radius at which the loss occurs, while on either side of it, the dashed lines show the distributions of four neighboring radial bins. The curves are vertically offset in order to distinguish the differences between them. For the local case (a), the distribution is reduced dramatically at the point of the loss, but only two radial bins away has recovered almost completely. In contrast, the nonlocal regime shows less depletion of the distribution at r' and the deficit is apparent at all r . The log scale of the figure masks the effect of the point source in both cases.

The results discussed above are different than those obtained in a one-dimensional solution, as shown in Figure 12. In a 1-D model, such as the local or nonlocal approximation, the distribution function is unable to recover from a point loss, and takes on a reduced form at all energies greater than ϵ'' . In the examples of Figure 11, both distributions recover at higher energies because electrons are able to flow around the loss point. These electrons feed the high-energy tail of the distribution, maintaining its overall shape. In a 1-D model, there is no way for the electrons to flow around the loss point; thus the distribution never recovers from the loss.

If point losses are included at all radial bins, generating a line-of-losses in the ϵ - r space, we obtain results analogous to the 1-D models. As explained above, the reason the distribution functions in Figure 11 recover at higher energies is because electrons are able to flow around the loss point, feeding the tail. Extending our model from a point loss to a line-of-losses impedes this flow. Once the loss extends across all radii, there is no longer a path to the high-energy tail, and the distribution takes on a reduced form identical to a 1-D result.

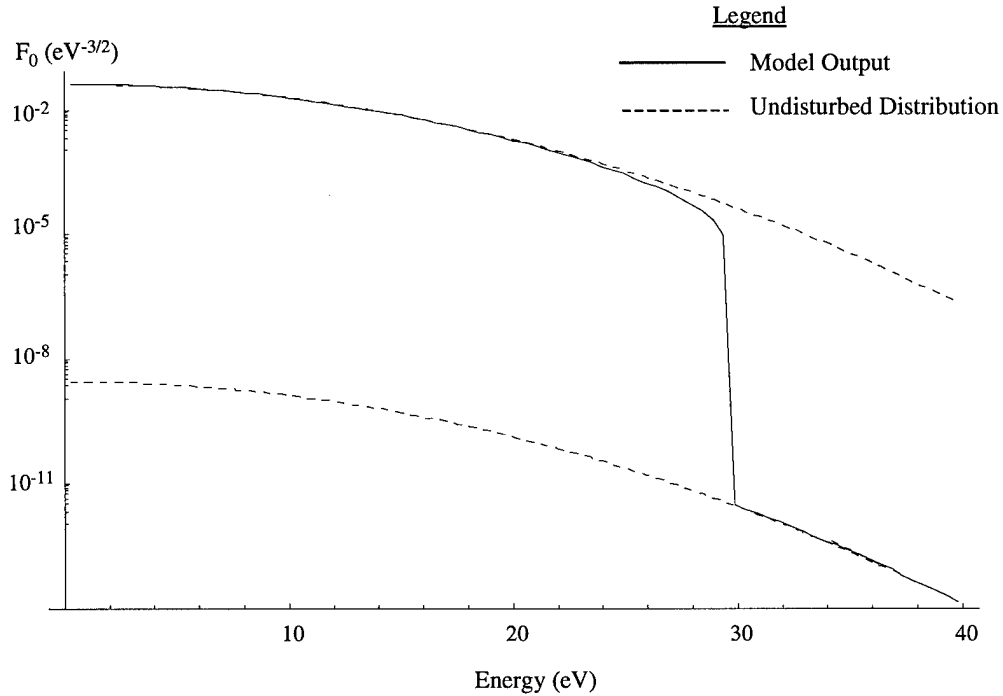


Figure 12 Log/linear plot of the EEDF versus energy for the case of a point source and an uninterrupted line-of-losses within the 2-D strict model. Model output is also equivalent to the result of a 1-D model with a single point loss. Dashed lines show undisturbed Druyvesteyn distributions.

Figure 12 displays model output for the case of a line-of-losses. Although only one radial location is shown, the effect is the same at all radii. In this figure, the solid line indicates the model output, while the dashed lines are undisturbed Druyvesteyn distributions. The lower curve has been shifted down to align it with the high-energy tail of the output. Notice that below 25 eV the output is unaffected by the loss-line. Where the loss occurs, there is a steep drop, then at energies above 30 eV the distribution recovers to the Druyvesteyn form, although reduced in magnitude. This is exactly the same behavior seen for a point loss in a 1-D model.

These limiting examples demonstrate the ability of the model to react to losses and gains within the system. They also serve once again to illustrate differences between the local and nonlocal regimes.

4.4. Phase IV: Completion of the Model

After gaining insight using artificial sources and losses, we were ready to add realistic collision terms and complete the model. This section discusses implementation details of the final solution.

By including inelastic collisions, the model moves from equation (41) to the full CBE, equation (10), and the associated difference equations in Appendix D. The addition of volumetric ionization requires us to choose one of the wall loss formalisms, (21) or (22), in order to assure a steady state solution. Having added this final functionality, the model itself is complete. However, in order to accurately model physical systems we must also specify physically representative input parameters.

A self-consistent model is one that uses only externally determined parameters such as the pressure in order to reach a solution. In the case of the positive column, a completely self-consistent model would require only: constituent gas data, gas partial pressures, axial field strength, and axial current. But the model, in its present form, is not self-consistent regarding three internal variables: the radial potential, excited state number density, and total wall loss. Therefore, in addition to the externally determined parameters, these three internal variables must be specified as well.

In the present model, values for the radial potential are either assumed or measured experimentally. In this thesis we use assumed forms exclusively, usually quadratic or cubic. Experimental data, if available, are preferred, but their use is limited to the specific parameters of the experiment. Another option is to first run a self-consistent nonlocal model, and then use the calculated potential as input to the strict

solution. While this method is only an approximation, in most cases it is probably more accurate than simply assuming a form.

A similar situation exists with the excited state number densities, which are used in the calculation of de-excitation collisions and Penning ionization (see section 3.1.2). These collisions can have a significant impact on the EEDF, if the excited state density is a large fraction of the total density. In most physically realistic cases however, we have seen that excited state neutrals represent a small fraction of the overall neutral population. We therefore feel confident using educated estimates for these values, rather than pursue a self-consistent treatment. Future extension of the solution to a quasi-self-consistent model is discussed in chapter VII.

Having estimated values for the radial potential and excited number density, we are left with one remaining internal variable – the total wall loss. While the wall boundary conditions (21) and (22) proscribe the form of the loss, both have parameters to adjust the total integrated loss. We use this parameter to adjust the total number of electrons in the system, i.e. adjust the magnitude of the EEDF. Increasing the total loss forces the number of electrons to increase as well, in order to maintain the steady state. If measurements of the axial discharge current are available, this adjustment allows us to match the computed axial current, equation (53), to the experimental value. Without these experimental measurements we are forced to estimate the value of the total wall loss and adjust the wall loss parameter accordingly.

V. Model Validation

To validate the completed model, we compare its output to previously published work as well as to available approximate models. Since our solution formalism closely follows the development of Uhrlandt and Winkler, comparison to their work should yield nearly identical results. In the limit of high and low pressure, we can verify our results against those of the local and nonlocal approximations, using code previously developed by Bennett [6]. Finally, we validate the model against a totally different method, namely the Monte Carlo simulation technique.

5.1. Exposition of Model Output and Comparison to Uhrlandt and Winkler Results

Output from our strict solution is compared to the work of Uhrlandt and Winkler [7] for a neon discharge. The parameters for the discharge are a column radius of $R_{\text{wall}} = 1.7$ cm, a gas pressure of 0.62 Torr, which corresponds to a density of $N_0 = 2.0 \times 10^{16} \text{ cm}^{-3}$, and an axial current of $I_z = 10$ mA. The axial field strength is 2.1 V/cm and the radial potential has a minimum at the wall of $V[r] = -21$ V. We chose to use the Uhrlandt wall loss condition (equation (21)), setting $a = -0.1$ and $A = 1.05 \times 10^{12}$ in order to satisfy the proscribed axial current. For inelastic collisions we considered two excited states of neon, a metastable (m) and resonance (r) level, each with population densities of $2 \times 10^{11} \text{ cm}^{-3}$. Further data for those two states are shown in Table 1.

Table 1 Electron/Atom and Atom/Atom Collision Data Used in Neon Discharge Calculations. Notation: *m* – metastable, *r* – resonance, *o* – ground state.

Electron/Atom Collision Process		Energy loss/gain (eV)	
Excitation	$\text{Ne}_o + e^- \rightarrow \text{Ne}_m + e^-$	-16.62	
	$\text{Ne}_o + e^- \rightarrow \text{Ne}_r + e^-$	-16.67	
De-excitation	$\text{Ne}_m + e^- \rightarrow \text{Ne}_o + e^-$	16.62	
	$\text{Ne}_r + e^- \rightarrow \text{Ne}_o + e^-$	16.67	
Ground State Ionization	$\text{Ne}_o + e^- \rightarrow \text{Ne}^+ + 2e^-$	-21.56	
Atom/Atom Collision Process		Rate Coefficient ($\text{cm}^3 \text{s}^{-1}$)	
Penning Ionization	$\text{Ne}_m + \text{Ne}_m \rightarrow \text{Ne}_o + \text{Ne}^+ + e^-$	z_{11}	3.4×10^{-10}
	$\text{Ne}_r + \text{Ne}_r \rightarrow \text{Ne}_o + \text{Ne}^+ + e^-$	z_{22}	3.4×10^{-10}
	$\text{Ne}_m + \text{Ne}_r \rightarrow \text{Ne}_o + \text{Ne}^+ + e^-$	z_{12}	6.8×10^{-10}

It is important to note a number of differences between the two implementations of this strict solution. Both solutions admit a generalized potential, but Uhrlandt used an experimentally derived form, while we chose a simple cubic since we didn't have access to the same data. In addition, Uhrlandt performed a side calculation to estimate the excited state number densities. Although our treatment does not include this side calculation, we based our excited densities on the published results of Uhrlandt. The input densities do not match exactly, because our model assumes they are uniformly distributed, while Uhrlandt allows them to vary with r . Even so the results are remarkably similar.

Figure 13 displays the three scalar components of the EEDF, $f_0[r,u]$, $f_r[r,u]$, and $f_z[r,u]$, at two different radii, $r = 0.6$ and $r = 1.2$ cm. While examples of the isotropic distribution, f_0 , have been shown previously, this is the first example of the radial and axial components. Note that at all radii, the axial component of the distribution is

negative, reflecting the action of the axial electric field, directed in $+\hat{z}$, to bias the electron's velocity in the $-\hat{z}$ direction. The radial distribution, on the other hand, undergoes a sign change. At lower energies, a positive f_r corresponds to a radial flux toward the wall, while at higher energies, f_r turns negative for much of the solution area, indicating flow away from the wall. At some point this high energy flow must reverse sign in order to satisfy the wall loss boundary condition; this is discussed further in Chapter VI.

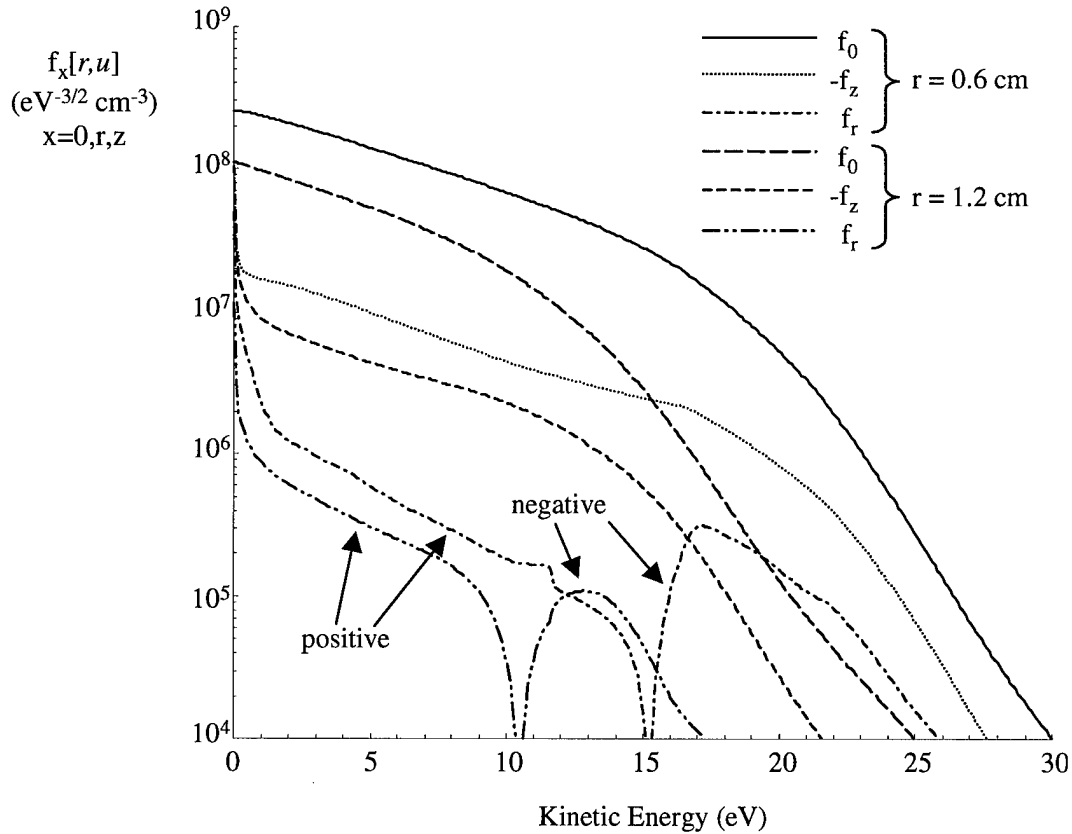


Figure 13 Log/linear plot of components of the EEDF, for the neon discharge at two radii, calculated using the strict solution: isotropic $-f_0[r, u]$, radial $-f_r[r, u]$, and axial $-f_z[r, u]$.

A comparison of Figure 13 with that found in the Uhrlandt paper [7, pg 537] shows excellent agreement for all three components. At both radial locations, the peak

magnitude of f_0 matches exactly with those in the Uhrlandt paper, and the overall forms of the distributions are identical. The two anisotropic components are also very similar; in Figure 13, f_r changes sign at energies of 10.5 and 15 eV, while in Uhrlandt's paper the reversal occurs at 11 and 15 eV. The anisotropic components also show many of the same small-scale variations in both figures.

While a graphical comparison of our EEDF to Uhrlandt's work is satisfying, more rigorous tests exist. From the distribution function, we derive a host of macroscopic observables, which are often the true quantities of interest (see Appendix A). Space does not permit us to display all of the results, but we obtained excellent agreement with Uhrlandt for quantities such as the electron number density, mean energy, and integrated currents. However, the most rigorous test of the model comes from looking at particle and energy balances. As presented in Appendix A, the particle balance, equation (54), equates the particles lost at a given radius (divergence of particle current) to the particles gained through ionization sources (ground and Penning ionization rate). Similarly, the energy balance, equation (55), compares the net energy leaving a given radius (divergence of the energy current) to that gained and lost from collision terms as well as the action of the axial and radial electric fields.

In Figure 14, we see a plot of the particle balance for the neon case considered. If the model achieves complete particle balance, the sum of the two ionization rates (ground state ionization and Penning ionization) will exactly equal the divergence of the particle current at each radial location. As seen in the figure, the total ionization rate for neon is everywhere slightly less than the net divergence. However, we obtained relative errors in the particle balance less than 2% for the majority of the tube, which is the same as that

reported by Uhrlandt. In the region between 0.9 and 1.2 cm, we see a greater deviation of approximately 12% in the balance that is as yet unexplained.

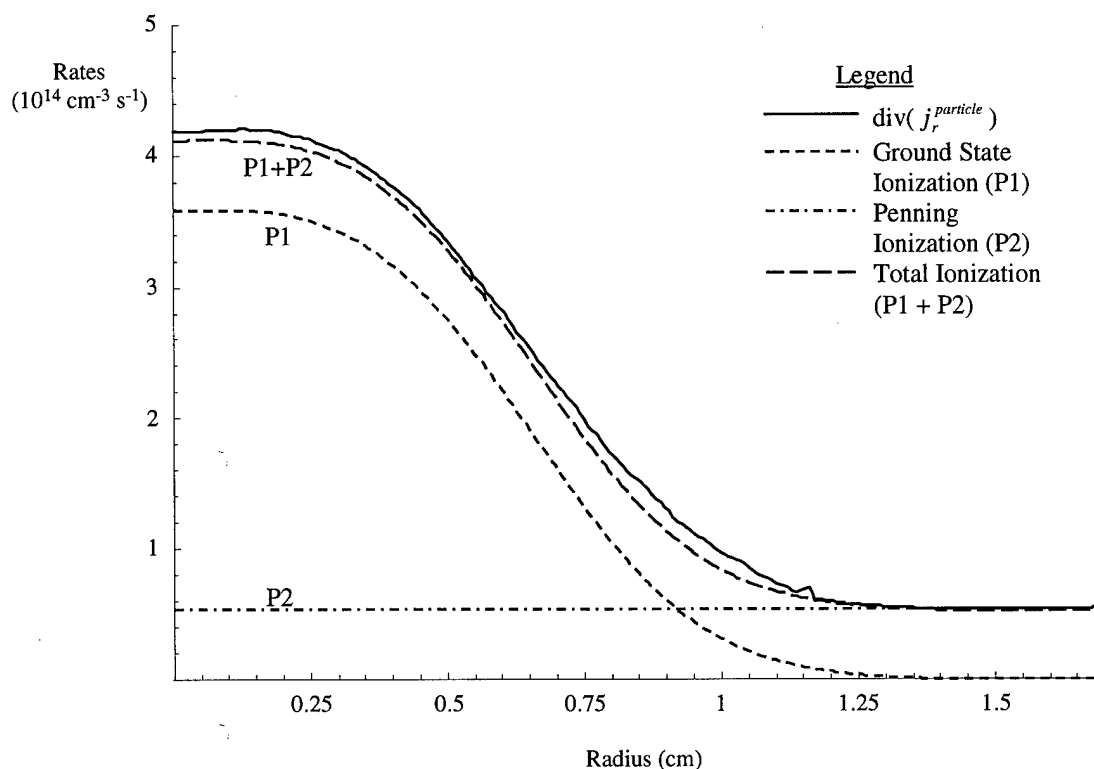


Figure 14 Terms in the electron particle balance as a function of radius for the case of a neon discharge.

If we compare Figure 14 to the equivalent figure in Uhrlandt's paper [7, pg 542], we notice immediately the difference in the Penning ionization treatment. As stated earlier, Uhrlandt included a radial dependence in the excited state species concentration, with a maximum on axis that decays to zero at the wall. Because of this, his Penning term reflects the same radial dependence, contributing zero at the wall. In our model however, the excited state species are uniformly distributed, which results in an equal Penning contribution at all radii.

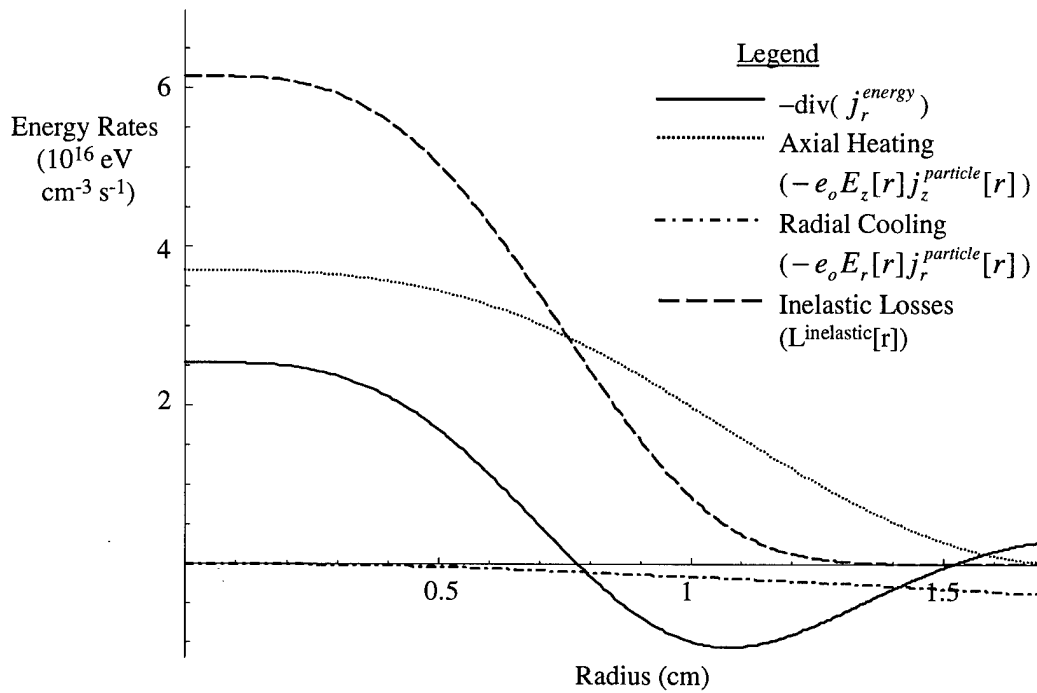


Figure 15 Important terms in the local energy balance as a function of radius for the neon discharge. Not shown are elastic collisional losses and inelastic collisional gains, which are insignificant in this case.

The radial energy balance is shown in Figure 15. As in the case of the particle balance, the divergence of the energy current should equal the sum of the various energy gains and losses at each radial location. It is important to note that the signs of the divergence and inelastic loss terms are reversed from equation (55) in an effort to condense the figure. As plotted, the divergence, axial heating, and radial cooling sum to give the inelastic loss. In addition, the magnitude of two terms, the losses due to elastic collisions (L^{elastic}) and the energy gains from collisions (G^c), are too small to appear in the figure.

Figure 15 also corresponds to a similar figure in Uhrlandt's paper [7, pg 543]. In his results, Uhrlandt quotes relative errors in the energy balance of less than 0.1%. For the neon case shown, this treatment achieved errors less than 0.5% for the majority of the

tube radius. Near $r = 1.2$ cm the divergence approaches zero, and the relative error increases dramatically; however, this is not considered an indication of any error in the model.

The figure above demonstrates why energy transport is observed from the outer to inner parts of the neon discharge. Near the axis, inelastic losses outweigh axial heating, but the terms reverse dominance at approximately $r = 0.75$ cm. Excess energy added near the wall thus moves toward the axis to fill the deficit there. Also interesting is the effect of the radial field. A net radial current flows outward to supply the wall loss; this flow is along the radial field, which (for negatively charged electrons) leads to a small radial cooling.

5.2. Verification Against the Local and Nonlocal Approximations

Local and nonlocal approximate models present another opportunity to validate our solution. While numerous published results exist, we have the capability to use “in-house” versions of these approximations developed by Bennett [6]. In this way we can ensure the input parameters are exactly the same. In addition, we are able to compare the model output directly rather than examine diagrams from a journal article.

In these tests we want to validate the strict model, not the approximations. With this in mind, the input parameters are chosen to create the conditions for which the respective approximations are most valid. As an example, neither approximation includes a mechanism for wall loss; thus for this validation, we employ the wall loss cone formalism, with the reflection coefficient set to 1 – total reflection. Without wall loss, we are also forced to neglect ionization sources, in order to satisfy the steady state requirement.

The model validation was made using neon as the neutral gas, with the same input parameters as used in the Uhrlandt comparison above, unless specified otherwise. We chose input values to guarantee that the system fell into the appropriate regime, local or nonlocal, when comparing to the respective models. Based on the results of equation (5), we consider the neon column local at a $PR = 50$ and nonlocal at $PR = 0.1$. Keeping the ratio of E_z/N constant, this leads to the following input parameters: local comparison – $P = 29.4$ Torr, $E_z = 99.6$ V/cm; nonlocal comparison – $P = 0.062$ Torr, $E_z = 0.21$ V/cm.

One difficulty that exists in the comparisons is that the local and nonlocal models use uniform gridding, while the strict model uses a non-uniform grid. Thus the output data do not coincide, and we can not calculate the relative error between specific solution points in the models. To overcome this, the output from both models is interpolated using cubic splines. The interpolation polynomials are then sampled uniformly, using the resulting data set to calculate the relative error.

Another consequence of the difference in gridding is how the cross section data is sampled. The elastic collision cross section of neon has a feature at low energies (the Ramsauer minimum) that influences the shape of the distribution function. The non-uniform grid technique (section 3.2.1) results in high resolution of this low energy feature, while for the same number of bins, the uniform grid could not resolve it. To correct this deficiency, the local and nonlocal models were run on a mesh with twice the number of energy bins as the strict solution.

Using the input parameters and methodology discussed above, the models were compared over a range of 30 eV and at three radial locations ($r = 0, 0.5$ and 1 cm). The results from the nonlocal case were uniformly impressive. The models deviated by no

more than 4% in relative error, while the distribution itself spanned over 4 orders of magnitude. In the local comparison, the results were equally impressive at the first two radial locations, with the relative error again below 4%. But at $r = 1$ cm, the wall boundary, the models deviated significantly. We believe this is due to the rapid decrease in the radial potential near the wall, which causes a breakdown in the local assumption of no radial variations over the electron energy relaxation length (section 2.2). As such, these errors reflect on the local approximation, and not the implementation of the strict solution.

5.3. Comparison to Monte Carlo Methods Using Argon

In the previous two sections we compared our strict kinetic solution results to those of other kinetic solutions. As a final check on the model, we look to a completely different technique for verification, Monte Carlo particle simulation. Specifically the strict solution is run under the conditions reported by Kortshagen et al. [9], in which they investigate the EEDF of an argon discharge.

As with the Uhrlandt comparison in section 5.1, we again try to match the input parameters to those stated in the paper. For the radial potential, Kortshagen assumed a quadratic form. At the wall boundary, he employed a Monte Carlo version of the loss cone boundary condition, assuming $\Delta\phi = 8$ eV and total absorption at the wall, $\chi = 0$. As explained in section 3.1.3., our treatment of the loss cone formalism differs slightly, incorporating the potential jump, $\Delta\phi$, as a steep increase in the radial potential just prior to the wall, rather than a step function at $r = R_{\text{wall}}$. Finally, Kortshagen made no mention of including the effects of Penning ionization or collisions of the 2nd kind, thus these features were turned off for the model comparison.

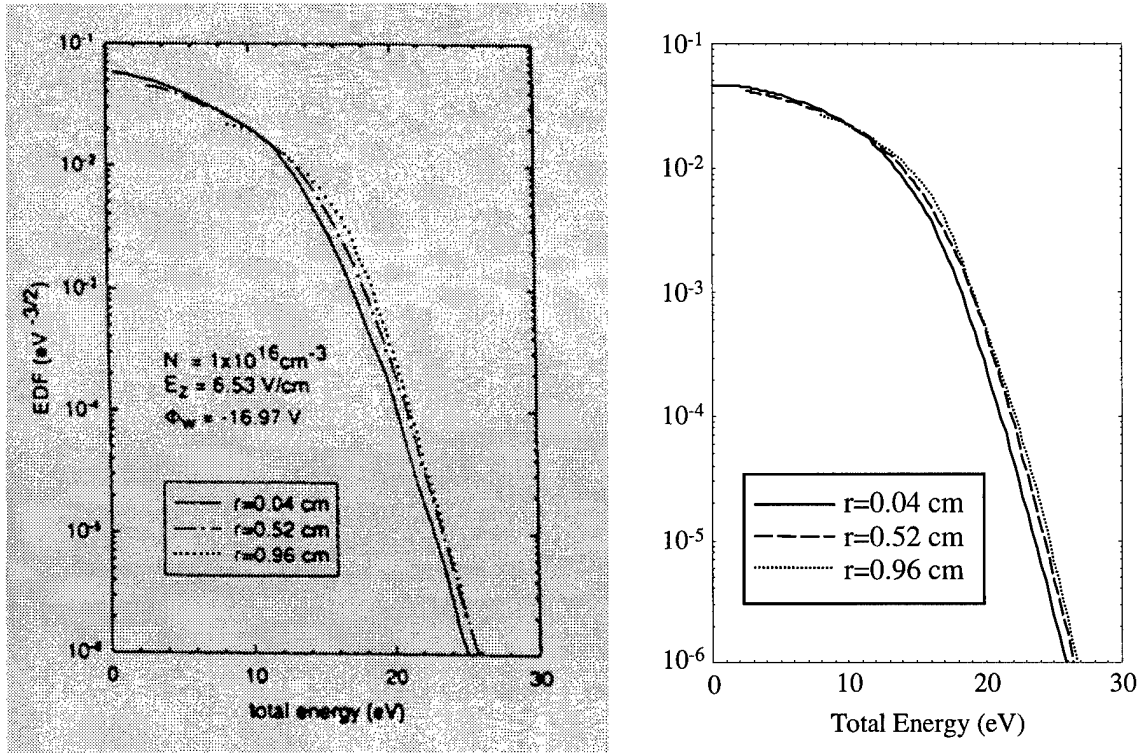


Figure 16 Comparison (a) of Monte Carlo calculation [9] (left) and strict solution, present work, (right) for an argon column at three different radii. Plotted is the EEDF as a function of total energy.

We compared the two models for two cases, (a) and (b); the relevant input parameters are given in Table 2. Figure 16 presents the results for the first comparison: on the left a photocopy from the Kortshagen paper, on the right the output from our strict model. A similar presentation is made in Figure 17 for the second set of input parameters.

Table 2 Input parameters for model comparisons between Monte Carlo and strict solutions in an argon column.

	Comparison (a)	Comparison (b)
Number density	$N = 1 \times 10^{16} \text{ cm}^{-3}$	$N = 3 \times 10^{16} \text{ cm}^{-3}$
Pressure	$P = 0.31 \text{ Torr}$	$P = 0.93 \text{ Torr}$
Axial Field	$E_z = 6.53 \text{ V/cm}$	$E_z = 12.4 \text{ V/cm}$
Sheath Potential	$V_{\text{sheath}} = -8.97 \text{ V}$	$V_{\text{sheath}} = -10.31 \text{ V}$
Wall Potential	$V_{\text{wall}} = -16.97 \text{ V}$	$V_{\text{wall}} = -18.31 \text{ V}$

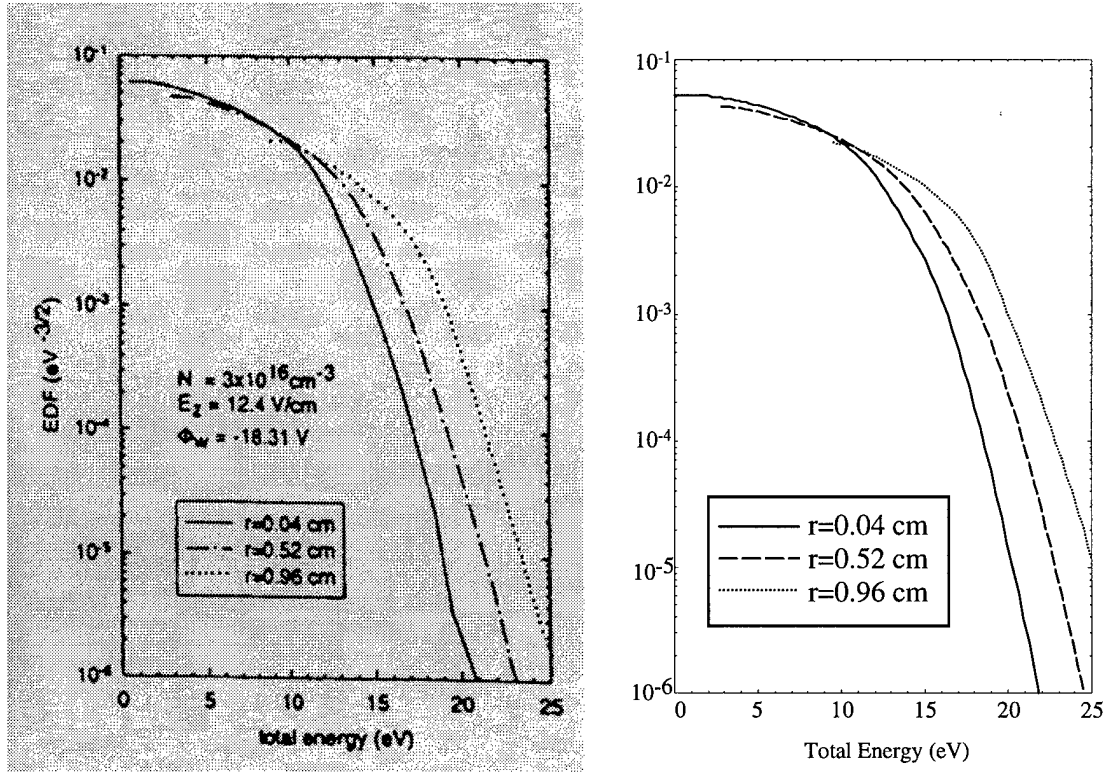


Figure 17 Comparison (b) of Monte Carlo calculation [9] (left) and strict solution, present work, (right) for an argon column at three different radii. Plotted is the EEDF as a function of total energy.

Although the two models use vastly different approaches to simulate the argon column, the results are remarkably similar. In Figure 16, the plots at all three radii follow almost exactly those of Kortshagen. In the second run, Figure 17, a slight deviation is noted for the EEDF at $r = 0.96$ cm, but this is attributable to our incorporation of the sheath potential increase, $\Delta\phi$, into the radial potential rather than as a step increase at the wall.

These results, combined with those of the previous two sections, demonstrate the accuracy of this strict kinetic model as compared to other well-established solutions.

VI. Investigation of Special Topics

As mentioned initially in the introduction, the main purpose of this thesis was to develop and validate the strict solution method. Continuing the theme, this chapter looks more closely at some of the characteristics of the strict solution. In doing so, we further our understanding of the solution and at the same time reveal interesting properties of the electrons kinetics in a glow discharge.

6.1. Current Flow within the Solution Space

An exciting consequence of the strict solution is that we can model radial current flow within the plasma. Since the approximate methods are one-dimensional and disregard wall loss, they result in no net radial flow. In this section, we revisit the results of the neon discharge discussed previously in section 5.1, using the same input parameters.

As listed in Appendix A, the radial and axial particle currents are derived from the anisotropic components of the EEDF by integrating the particle flux over energy (equation (48)). Considering the differential flux, we can map electron flow within the solution grid. Figure 18 presents a vector field plot of the electron flux, or differential particle current, within the neon solution area. The figure is constructed by combining the radial and axial flux components into a vector; all of the vectors are then scaled to the same length. Unfortunately, this scaling removes all information about the magnitude of the vectors. Note that, although it is not apparent from the figure, the differential flux becomes negligibly small in the upper left corner of the solution grid.

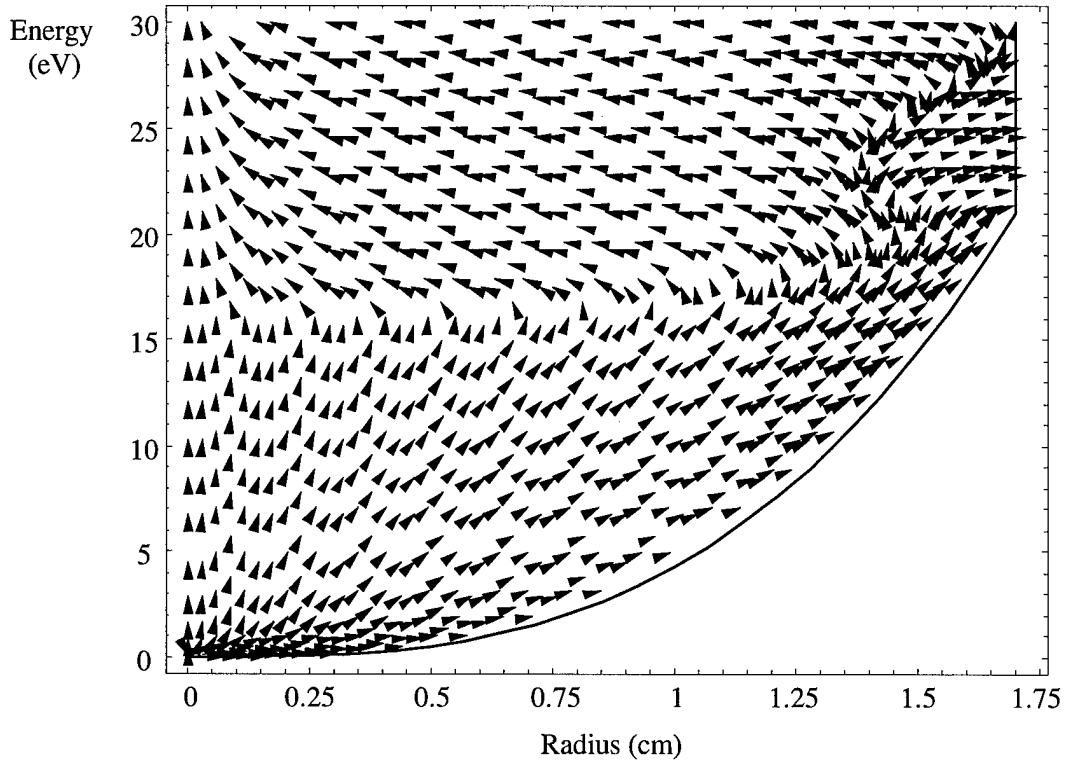


Figure 18 Vector diagram of electron flux within the neon discharge solution area.

Three mechanisms contribute to create a particle flux circuit in the solution space shown in Figure 18: particle diffusion, the action of the radial electric field, and inelastic collisions. Starting near the origin of the diagram, we see that diffusion dominates, driving low energy electrons toward the wall, along (but against the influence of) the radial electric field. Diffusion therefore produces a small cooling of the electrons. At the edge of the tube, some high-energy electrons exit the system via the wall boundary condition. The rest reverse course and head back toward the axis, driven now by the radial electric field. To complete the circuit, inelastic collisions scatter high-energy electrons back to lower energies. The majority of this scattering takes place near the axis, because, for a given total energy, electrons there have the greatest kinetic energy. Of course, against the backdrop of all this radial flow is the constant action of the axial field, driving electrons to higher energies.

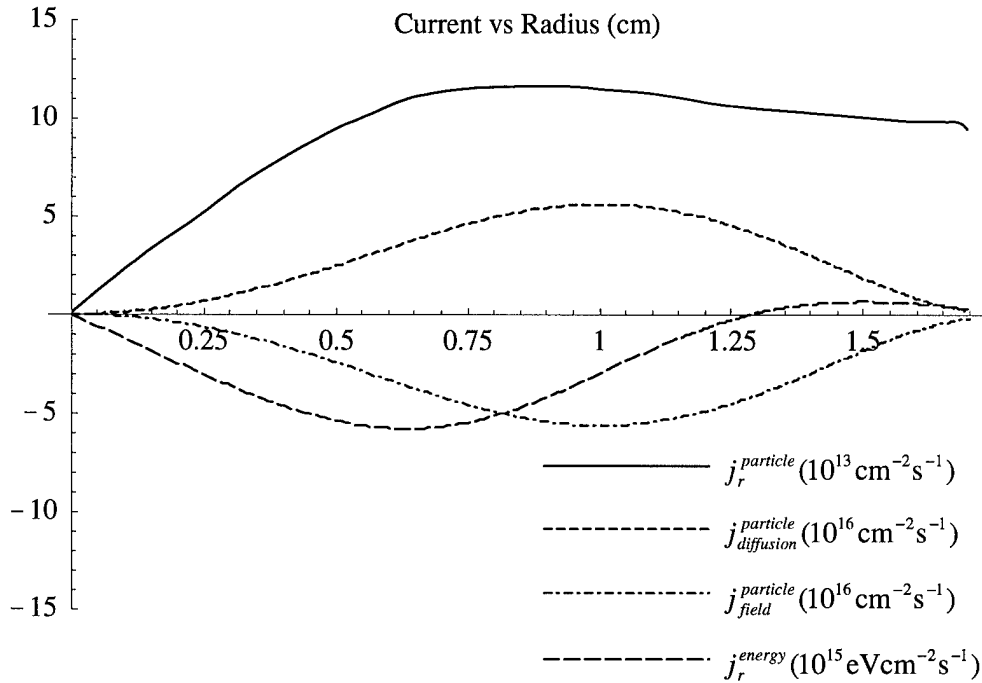


Figure 19 Integrated current flows within the neon discharge, plotted as a function of the tube radius.

A complementary view, Figure 19, displays the currents for the same neon column; these currents are found by integrating the differential flux shown in Figure 18 over energy (equations (48) - (52)). The net radial current, $j_r^{particle}$, is the sum of two components: the flow due to diffusion, $j_{diffusion}^{particle}$, and that due to the radial electric field, $j_{field}^{particle}$. As described earlier, the diffusion current is comprised of low energy electrons moving toward the wall, while high-energy electrons make up the field driven current. Notice that the diffusion and field driven currents are nearly equal and opposite, although when summed, they result in the net positive particle current ($j_r^{particle}$), which supports the wall loss. While the net current is positive, most of the high-energy electrons are moving towards the axis, resulting in a negative energy current (j_r^{energy}). Only near the wall, where all of the current becomes positive, does the energy current change sign.

It is important to reiterate that only through the 2-D strict solution are we able to investigate these radial currents.

6.2. Applicability of the Approximate Methods

The strict kinetic method provides a robust and flexible model of the EEDF, but it is computationally demanding. Because of this, we might be tempted to employ one of the approximate kinetic methods, if they are valid. As discussed in Chapter II, the local (nonlocal) approximation is applicable when the electron energy relaxation length is much less (greater) than the tube dimensions. While expressions such as (5) attempt to formalize this requirement, they do not provide absolute guidance concerning when the approximate solutions may be used. Ingold suggests a general range of applicability, which is listed in Table 3.

Table 3 Range of validity for models of interest [8, pg 5943].

Method	$PR < 1$	$1 < PR < 10$	$10 < PR < 100$
Strict Kinetic	Yes	Yes	Yes
Nonlocal Approximation	Yes	?	No
Local Approximation	No	No	?

We know that neither approximate solution will be accurate for all r , because neither includes a wall loss. The nonlocal approximation assumes that $\frac{\partial f_0}{\partial r} = 0$ everywhere, which is violated for any nonzero wall loss since $f_r \propto \frac{\partial f_0}{\partial r}$. Furthermore, in the local case, the radial potential varies rapidly in the vicinity of the wall (Figure 2, page 8), which violates the assumption that the electron relaxes in energy space before conditions change radially. The question therefore, should not be “when are the approximate methods valid?”, but “how accurate can we expect them to be?”

We have already shown in section 5.2 that in their regimes of applicability, both the local and nonlocal approximations yield results within 4% of the strict solution over at least half the tube radius. However, in that validation phase the rather unrealistic condition of zero wall loss was chosen to minimize the differences in the models; we now wish to revisit the question using a more stringent evaluation.

Because our strict solution accurately spans both high and low pressure regimes, we can use it alone to determine the validity of the nonlocal and local approximations. For instance, in the nonlocal approximation, the EEDF is a function of total energy only. Thus, to test the “nonlocality” of the system, we simply compare the values of f_0 at different radii, keeping ε constant. If the system is completely nonlocal, then the relative difference between $f_0[r_1, \varepsilon_1]$ and $f_0[r_2, \varepsilon_1]$ will be zero. Deviations from nonlocality correspond to errors in the approximation and hence, errors inherent in the nonlocal model. We can therefore use the deviations to gauge the accuracy of the approximation.

As in section 5.2, we ran the tests for a neon column. The following parameters were used: $R_{\text{wall}} = 1$ cm, a quadratic potential with $\phi[R_{\text{wall}}] = 20$ V, and a loss cone condition with $\chi = 0.5$. The resulting data are presented in Table 4. It shows the maximum relative difference between f_0 on axis and at three other radial values; this deviation is also mapped as a function of PR value.

Table 4 Deviation from nonlocality (relative percent) for a neon column as a function of PR value and radius.

PR (Torr-cm)	$r = 0.5 R_{\text{wall}}$	$r = 0.75 R_{\text{wall}}$	$r = R_{\text{wall}}$
0.01	< 1%	< 1%	1%
0.05	1%	3%	7%
0.1	3%	6%	14%
0.5	2%	10%	46%

The results in Table 4 show that the applicability of the nonlocal approximation depends not only on PR , but radius as well. Note the disparity between these results and the general guidance in Table 3. According to Ingold, the nonlocal approximation is valid for $PR = 0.5$, but in our tests at $r = R_{\text{wall}}$ the relative error is 46%. In all cases the maximum deviations from nonlocality occur in the high energy tail of the distribution function, reflecting in part the effect of the wall loss boundary condition.

It is also interesting to compare how other gases react to the test of nonlocality. For neon, equation (5) gives an approximate PR value of 17 Torr-cm. Argon, on the other hand, results in a value of ~ 6 Torr-cm. We therefore expect that for the same PR value, an argon column will have greater deviations from nonlocality than neon. Table 5 shows the results of the argon column using the same parameters as for neon. As expected, the deviations are much greater in each case.

Table 5 Deviation from nonlocality (relative percent) for an argon column as a function of PR value and radius.

PR (Torr-cm)	$r = 0.5 R_{\text{wall}}$	$r = 0.75 R_{\text{wall}}$	$r = R_{\text{wall}}$
0.01	1%	3%	7%
0.05	4%	8%	30%
0.1	14%	22%	35%
0.5	96%	99%	100%

We can make similar comparisons in the local regime. If the column satisfies the local approximation exactly, the normalized EEDF will be the same at all r regardless of the radial potential, i.e. $f_0[r_1, u]/n_e[r_1] = f_0[r_2, u]/n_e[r_2]$. Unfortunately, in this case we are comparing f_0 at constant u , which means that the grid points do not coincide. To work around this problem, we employ the same technique as in section 5.2, interpolating the data and then re-sampling it uniformly to calculate the relative errors. This technique

worked well for the neon column, but failed for argon. The failure stemmed from the inability of the spline interpolation routine to adequately fit the model output over the 40-decade drop in the distribution function. The spline routine returned a highly oscillatory fit that resulted in extremely large relative errors. So we ran the comparison for neon only, using the same input parameters as above.

Table 6 Deviation from locality (relative percent) for a neon column as a function of PR value and radius.

PR (Torr-cm)	$r = 0.5 R_{\text{wall}}$	$r = 0.75 R_{\text{wall}}$	$r = R_{\text{wall}}$
10	19%	55%	350%
50	7%	23%	145%

The most important observation from the data above is how poor the local approximation is at $r = R_{\text{wall}}$. This again relates to the fact that near the wall, two assumptions are violated. First, as mentioned in section 2.2, at the wall the radial electric field is not negligible compared to the axial field. And second, the potential varies rapidly in this area, violating the assumption of radial homogeneity over the scale of an electron mean free path.

After including the effects of wall loss, it is apparent from the data above that the approximate methods are limited to a range of pressure, as well as a fraction of the tube radius.

6.3. Effect of the Wall Loss Boundary Condition

As first explained in section 3.1.3, the wall loss boundary condition is an extremely important, yet almost arbitrary restriction on the solution. We choose simple expressions to represent the loss, masking the true nature of this problem, which involves complicated physical processes including ion/electron recombination, absorption, and

reflection [20]. While the wall loss cone has some physical basis, both it and the wall loss function largely neglect these complicated processes.

In his paper, Uhrlandt mentions that he tested a number of different forms for the loss function, including various exponential and trigonometric functions, but found that in general they “yielded almost the same results for the EVDF except for the region very near to the wall” [7]. In our studies, we found that while this statement was true for the two cases Uhrlandt presented, it is not true in general.

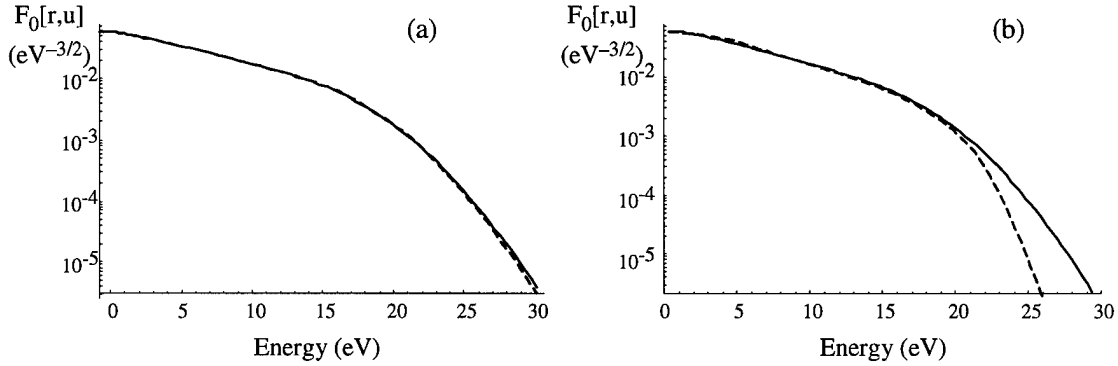


Figure 20 Comparison of the on-axis EEDF for the wall loss cone (dashed) and wall loss function (solid) at two PR values: (a) $PR = 1.0$ and (b) $PR = 0.1$.

Both of Uhrlandt’s studies considered gases in which the PR value was greater than one. As shown in Figure 20(a), for $PR \sim 1$, the two boundary conditions are indeed very similar far away from the wall. However, as we should expect from the earlier discussions of the nonlocal regime, at low PR , the EEDF is a function of total energy only, and any differences that exist at the wall are reflected on axis as well. Part (b) of the figure shows that at $PR \sim 0.1$ the solutions diverge significantly, even on axis. We thus need the “insulation” provided by high PR to confine our uncertainties in boundary condition to the region near the wall.

Within Uhrlandt's wall loss function, it is interesting to look more closely at how different choices for the parameter a (equation (21), page 29) effect the form of the EEDF. As explained earlier, we used $a = -0.1$ throughout this thesis, as Uhrlandt did in his treatment, but we never gave a physical justification for this choice. The parameter A , on the other hand, is chosen at run-time so the output matches experimental data (section 4.4).

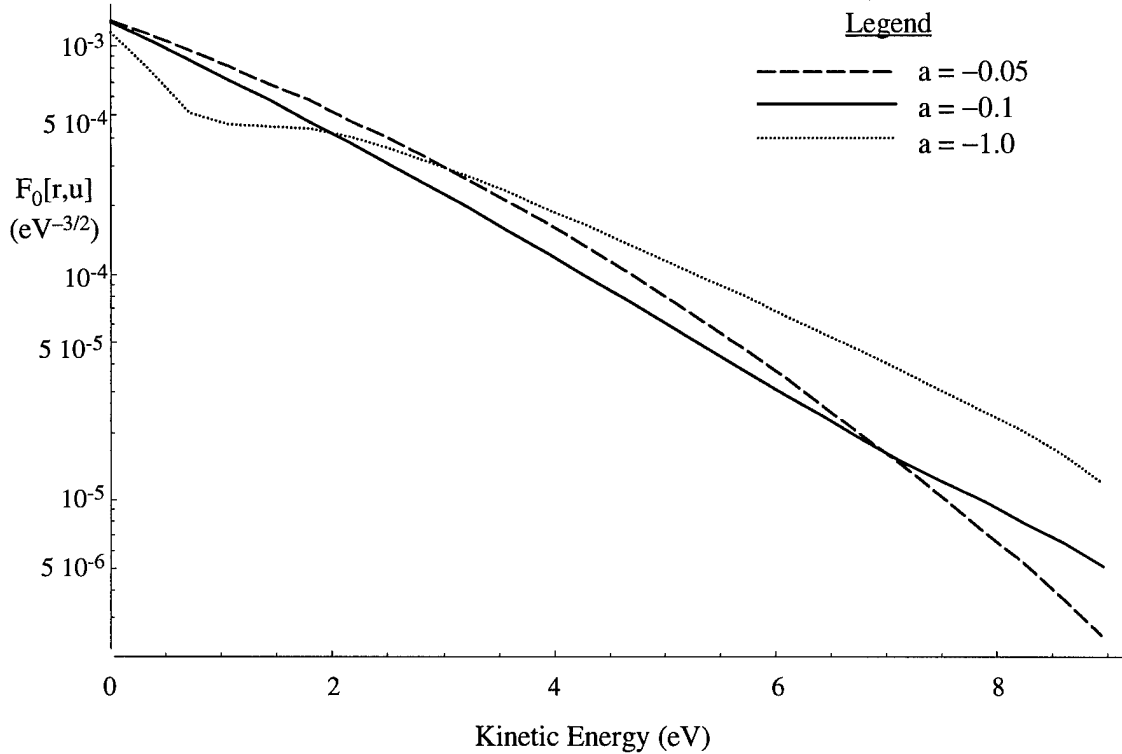


Figure 21 Isotropic component of the EEDF at $r = R_{\text{wall}}$ for three different values of the wall loss function parameter a .

Figure 21 illustrates how three different values of the parameter a effect the shape of the isotropic component of the EEDF, for $PR = 1$. As the magnitude of a increases, the exponential loss function drops more quickly to zero with increasing energy; thus to support a fixed loss, the majority of the loss occurs at low energies. On the other hand, as a decreases the loss function diminishes less rapidly with energy, and hence more of the

loss occurs at high energies. This effect is reflected in the sharp dip seen in the EEDF at low energies for $a = -1.0$, as opposed to the sustained decrease seen for $a = -0.05$.

Since the wall loss function is arbitrary, and only loosely physically based, we really have no basis for one choice of a over another. In the end, it comes down to aesthetics. From the figure, we see that when $a = -0.1$, the model produces an EEDF which is smooth and relatively flat on a log scale. In addition, this particular choice produces an EEDF similar to that given by the approximate methods; it thus has the shape we have come to expect. Other choices for a , especially $a = -1.0$, produce distortions, which without any physical justification to use them, we choose not to accept.

VII. Conclusions and Recommendations

7.1. Conclusions

The primary objective of this thesis was to implement and test a strict kinetic solution to the CBE of a glow discharge. We have achieved this goal, and thus fashioned a powerful tool to explore the electron kinetics of weakly ionized non-equilibrium gases. In the process, we developed numerical techniques that are directly applicable to the solution of related PDEs and gained insight into the applicability of other approximate kinetic models. Furthermore, we treated important mechanisms such as radial particle and energy transport, which are neglected in the approximations.

The general numerical techniques discussed in chapter III comprise a robust set of tools applicable to a variety of numerical problems. In section 3.2.1, we presented a method to generate non-uniform grids over a variable solution area. This gridding scheme required us to develop non-uniform differencing equations, as well as special counting variables to access the points in the solution grid. In section 3.2.3, we discussed our use of publicly available algorithms to solve sparse banded matrices and detailed an efficient memory storage scheme for the model. Our treatment of the resulting system of equations reduced the computational load significantly over “brute-force” methods.

During the course of the investigation we frequently validated our model against approximate kinetic methods. We saw that, given the proper assumptions, the strict solution matched very closely both analytic (section 4.1 and 4.2) and numerical results (section 5.2) of the local and nonlocal approximations. In later investigations however, we recognized that for realistic systems, the approximate methods failed to adequately

describe the entire solution area, due in large part to their lack of a wall loss condition (section 6.2). We concluded therefore, that only a strict solution provides a complete description of the positive column, especially at the operating pressures of today's physical devices.

Throughout the validation and investigation phases of the thesis, we repeatedly demonstrated the necessity of employing a two-dimensional solution. It was only through this strict solution that we were able to properly account for radial current flows and energy transport, and explain such phenomenon as radial electron cooling and the negative energy current in a neon column.

After devoting much of this thesis to the development and validation of the strict kinetic model, we have only begun to demonstrate its capabilities. The material presented here accounts for a mere fraction of the possible permutations. In fact, we considered only single species atomic gases throughout the treatment, but our solution also accommodates gas mixtures and molecular gases⁶. In its present form, practical applications for the solution are enormous. The model is ready to be used to optimize the kinetic design of lighting, electric discharge lasers, and plasma processing devices. But development should not end here. As mentioned previously in the Introduction, this research marks a first generation effort toward the future exploitation of plasmas in modifying aircraft flight characteristics. With this goal in mind, a number of model extensions are recommended as future research projects.

⁶ We are able to treat molecular gases by including the vibrational and rotational energy level cross-sections and increasing the energy grid density in order to resolve the finer details of these interactions.

7.2. Recommendations for Future Work

The most obvious extension of the model is to make it time dependent, rather than steady state. This modification only involves the inclusion of one additional term into the CBE. And as noted in section 3.2.3, our current numerical technique is well suited to employ this time dependence. By adding time dependence, the solution could then be used to investigate wave propagation as well as plasma instabilities in the positive column.

A more radical variation would be to switch from a study of radial to axial kinetics. The present solution models the axially homogenous positive column region of the glow discharge, but a change in coordinates would allow investigation of axial inhomogeneities. One practical use for this is the study of shocks in a discharge tube. Shocks can be modeled by rapid variations in the constituent number density and resulting space charge field. Our current solution accepts a general potential, which in the new problem would allow for a jump in the electric field strength; however, the model does not include a mechanism to vary the number density spatially. We could add a spatial dependence to the density in two ways, either as a constantly varying parameter like the potential, or as a step function, taking on two different values, one on either side of the shock. The most difficult part of the transition would be to specify appropriate conditions at the two spatial boundaries. Unlike the cylindrical case, there are no symmetries to take advantage of at these boundaries. One possible technique would be to specify the absolute axial flux at both boundaries, similar to Uhrlandt's wall loss function.

Further modifications to the code would allow us to investigate an even wider class of physical problems. As an example, the solution method could be applied to studies in the space environment. As with shocks in a discharge tube, after a simple change of coordinates and boundary conditions, we should be able to employ the strict solution technique to solve for the EEDF and resulting macroscopic quantities. Of course in this case, we would also need to add a magnetic field to the acceleration terms.

During the development of our solution, we noted a number of limitations to the model, some of which could also be the subject of future research. The two most important involve the excited state number densities and the radial potential. In both cases, the current solution method does not solve for these parameters self-consistently; rather it leaves them as variables to be determined through experiment or supplementary analysis.

Uhrlandt and Winkler have employed a quasi-self-consistent technique that solves for the excited state number densities. Their technique uses a complementary calculation to the strict solution, adjusting the excited state densities iteratively after a rate balance analysis [7]. In order to add this functionality to our model, the first step would be to make the excited state number density a function of radius. With the radial variation included, the next step would be to add Uhrlandt's rate balance analysis as a new component to the existing code. Once included, the modified code would require an iterative approach, starting with an assumed form for the number densities and updating the fraction of excited neutrals after each iteration, until the computed axial discharge current converges on an experimental or expected value.

The radial potential also presents an opportunity for future work. To date no one has performed a self-consistent strict solution for the radial potential, although Bennett [6] has done so for the nonlocal approximation. In order to incorporate this calculation, we would have to simultaneously determine a radial distribution for the ions as well as the electrons. The resulting distributions would then be used to solve Poisson's equation for the radial potential. While we could theoretically write a CBE for the ions and solve it directly, Bennett has shown that for the conditions of interest a far more simple technique is to employ a fluid analysis for the ions, while solving for the electron distribution directly. This is analogous to the method Uhrlandt used in his treatment of excited state number densities. After including the fluid calculation into the code, the solution proceeds iteratively, starting with an assumed form for the radial potential and updating it after each calculation, until it converges on a self-similar form.

In both these self-consistent treatments, as well as any time dependent approach, a limiting factor on the model's usefulness is program run-time. We mentioned in section 3.2.3, that the current code actually calls two algorithms. The first, and most computationally intensive, finds the LU decomposition of the input matrix (\mathbf{A}), while the second uses that result along with the forcing vector to solve the system of equations. If, between iterations or time-steps, the \mathbf{A} matrix does not change much, we can bypass the decomposition and solve the system quickly. In practice we might update the matrix only once every 5 or 10 iterations or time-steps, vastly reducing the overall run-time. Even so, both the self-consistent and time dependant problems will require much more computing power than used in this thesis.

Appendix A Macroscopic Quantities Derived from the Distribution Function

While the result of solving (10) is the isotropic distribution function, as a practical matter we are more concerned with macroscopic quantities such as the axial current, ionization rate, and electron mean energy. Not only are these the quantities used to design functioning equipment, but they constitute the easiest values to compare our results to other published works.

All of the macroscopic quantities are derived from an energy space integration over one of the three distribution functions f_0 , f_r , or f_z , where the anisotropic distributions are given by equations (15) and (16) respectively. Averaging over f_0 leads to the electron density, $n_e[r]$, the mean energy, $u_e[r]$, and the mean electron collision rates $P_{kl}[r]$:

$$n_e[r] = \int_0^{\infty} f_0[r, u] u^{1/2} du \quad (42)$$

$$u_e[r] = \int_0^{\infty} f_0[r, u] u^{3/2} du / n_e[r] \quad (43)$$

$$P_{kl}^{process}[r] = \sqrt{\frac{2}{m_e}} \int_0^{\infty} N_k Q_{kl}^{process}[u] f_0[r, u] u du \quad (44)$$

The mean ionization collision rate is found by substituting $Q_k^{ionization}$ into (44), with analogous substitutions to determine the excitation and de-excitation rates.

Energy loss densities associated with elastic and inelastic processes are given by,

$$L^{elastic}[r] = \sum_k \frac{2m_e}{M_k} \sqrt{\frac{2}{m_e}} \int_0^{\infty} N_k Q_k^{elas}[u] f_0[r, u] u^2 du \quad (45)$$

$$L^{inelastic}[r] = \sum_k \sum_l u_{kl}^{excitation} P_{kl}^{excitation} + \sum_k u_k^{ionization} P_k^{ionization}[r] \quad (46)$$

and associated energy gains determined from

$$G^c[r] = \sum_k \sum_l u_{kl}^{de-excitation} P_{kl}^{de-excitation}[r] + \sum_k \sum_{k^*} u_{kk^*}^{Penning} P_{kk^*}^{Penning}[r] \quad (47)$$

Using the anisotropic components of the distribution, we obtain particle and energy current densities

$$j_x^{particle}[r] = \frac{1}{3} \sqrt{\frac{2}{m_e}} \int_0^\infty f_x[r, u] u du \quad (48)$$

$$j_x^{energy}[r] = \frac{1}{3} \sqrt{\frac{2}{m_e}} \int_0^\infty f_x[r, u] u^2 du \quad (49)$$

where x refers to either r or z . The radial particle current is composed of two parts,

$$j_r^{particle}[r] = j_{diffusion}^{particle}[r] + j_{field driven}^{particle}[r] \quad (50)$$

$$j_{diffusion}^{particle}[r] = -\frac{1}{3} \sqrt{\frac{2}{m_e}} \int_0^\infty \frac{1}{K[r, \epsilon]} \frac{\partial}{\partial r} [f_0[r, u]] u du \quad (51)$$

$$j_{field driven}^{particle}[r] = \frac{1}{3} \sqrt{\frac{2}{m_e}} \int_0^\infty \frac{e_o E_r[r]}{K[r, \epsilon]} \frac{\partial}{\partial u} [f_0[r, u]] u du \quad (52)$$

where $K[r, \epsilon]$ is given by (83). The total axial discharge current is given by

$$I_z = -2\pi e_o \int_0^{R_{wall}} j_z[r] r dr \quad (53)$$

Finally, the solution is checked for self-consistency using particle and energy balances. The local particle balance equation for electrons is

$$\frac{1}{r} \frac{d}{dr} (r j_r^{particle}[r]) = \sum_k P_k^{ionization}[r] + \sum_k \sum_{k^*} P_{kk^*}^{Penning}[r] \quad (54)$$

And the local electron energy balance is given by

$$\frac{1}{r} \frac{d}{dr} (r j_r^{energy}[r]) = -e_o E_r[r] j_r^{particle} - e_o E_z[r] j_z^{particle} + G^c[r] - L^{elastic}[r] - L^{inelastic}[r] \quad (55)$$

Appendix B Derivation of Strict Solution Equations

This appendix presents a more thorough derivation of the equations given in section 3.1.1. It is based entirely on the previous developments of Holstein [10, 12] and Allis [13, 21]. As in section 3.1, the derivation begins with the collisional Boltzmann equation,

$$\frac{\partial f}{\partial t} + \vec{v} \cdot \vec{\nabla}_r f + \vec{a} \cdot \vec{\nabla}_v f = \left(\frac{\partial f}{\partial t} \right)_{\text{collision}} \quad (56)$$

where $f = f[\vec{r}, \vec{v}, t]$ is the electron velocity distribution function (EVDF); the other terms are described more fully on page 17.

The treatment in this thesis considers a steady state solution, in which case

$\frac{\partial f}{\partial t} = 0$. In addition, the only applied force is an electric field, which has both a radial

and axial component, thus $\vec{a} = -\frac{e_o}{m} \vec{E}$.

Under the conditions described in section 3.1.1, we make the assumption that the EVDF is nearly isotropic, allowing an expansion in spherical harmonics. Keeping only the first two terms gives

$$\begin{aligned} f[\vec{r}, \vec{v}] &= \sum_l P_l(\cos[\theta]) f_l(\vec{r}, \vec{v}) \\ &\equiv f_0 + \frac{\vec{v} \cdot \vec{f}_1}{v} \end{aligned} \quad (57)$$

where f_0 is the isotropic part of the distribution, and $\vec{f}_1[\vec{r}, \vec{v}] = f_r \hat{e}_r + f_z \hat{e}_z$ is the anisotropic part.

The next step is to substitute the results of (57) into (56) and simplify the result.

Considering each piece separately, we have for the radial flux term

$$\vec{v} \cdot \vec{\nabla}_r f = |\nu| \nabla_r (\cos[\theta] f) = |\nu| \nabla_r \sum_l \cos[\theta] f_l P_l[\cos[\theta]] \quad (58)$$

Using the identity,

$$\cos[\theta] P_l[\cos[\theta]] = \frac{(l+1)P_{l+1} + lP_{l-1}}{2l+1} \quad (59)$$

equation (58) becomes

$$\vec{v} \cdot \vec{\nabla}_r f = |\nu| \nabla_r \sum_l f_l \left\{ \frac{(l+1)P_{l+1} + lP_{l-1}}{2l+1} \right\} \quad (60)$$

Since this is an infinite series, we are free to re-index it to a new l , and then take two terms in the series.

$$\begin{aligned} &= |\nu| \nabla_r \sum_l P_l \left\{ \frac{l f_{l-1}}{2l-1} + \frac{(l+1) f_{l+1}}{2l+3} \right\} \\ &= |\nu| \nabla_r \left(\frac{P_0 \tilde{f}_1}{3} + f_0 P_1 + \frac{2 f_2 P_1}{5} \right) \\ &= |\nu| \nabla_r (f_0 \cos[\theta] + \tilde{f}_1/3) \\ &= |\nu| \nabla_r \cos[\theta] f_0 + |\nu| \vec{\nabla}_r \cdot \tilde{f}_1/3 \\ \vec{v} \cdot \vec{\nabla}_r f &= \vec{v} \cdot \nabla_r f_0 + \nu \vec{\nabla}_r \cdot \tilde{f}_1/3 \end{aligned} \quad (61)$$

Where we made use of the definition of P_1 , and the term f_2 was dropped since we are considering only a two-term expansion.

The energy flux term in equation (56) is tackled in a similar fashion, although we first need to rewrite the expression $\vec{\nabla}_v$. Assume we align a hypothetical z axis along the same direction as \vec{a} , then only the z component of $\vec{\nabla}_v f$ will contribute to $\vec{a} \cdot \vec{\nabla}_v f$. For that case we write,

$$\begin{aligned}
\vec{\nabla}_v &= \frac{\partial}{\partial v_z} \\
v_z &= v \cos[\theta] \\
\vec{\nabla}_v &= \frac{\partial v}{\partial v_z} \frac{\partial}{\partial v} + \frac{\partial \cos[\theta]}{\partial v_z} \frac{\partial}{\partial \cos[\theta]}
\end{aligned} \tag{62}$$

and use further relations to recast the term $\frac{\partial v}{\partial v_z}$,

$$\begin{aligned}
v^2 &= v_x^2 + v_y^2 + v_z^2 \\
\frac{\partial v}{\partial v_z} &= \frac{v_z}{v} = \cos[\theta]
\end{aligned} \tag{63}$$

We also recast $\frac{\partial \cos[\theta]}{\partial v_z}$

$$\frac{\partial \cos[\theta]}{\partial v_z} = \frac{\partial}{\partial v_z} \frac{v_z}{v} = \frac{1}{v} - \frac{v_z^2}{v^3} = \frac{1}{v} (1 - \cos^2[\theta]) = \frac{\sin^2[\theta]}{v} \tag{64}$$

then combine both results with (62) to give

$$\vec{\nabla}_v = \cos[\theta] \frac{\partial}{\partial v} + \frac{\sin^2[\theta]}{v} \frac{\partial}{\partial \cos[\theta]} \tag{65}$$

Continuing the assumption of alignment along \vec{a} , and using the results above, we are able to write the energy flux term in (56) as

$$\vec{a} \cdot \vec{\nabla}_v f = a \frac{\partial f}{\partial v_z} = a \left(\cos[\theta] \frac{\partial f}{\partial v} + \frac{\sin^2[\theta]}{v} \frac{\partial f}{\partial \cos[\theta]} \right) \tag{66}$$

Now make use of fundamental identities for Legendre polynomials

$$\cos[\theta] P_l = \frac{(l+1)P_{l+1} + lP_{l-1}}{2l+1} \tag{67}$$

$$\sin^2[\theta] \frac{\partial P_l}{\partial \cos[\theta]} = \frac{l(l+1)(P_{l-1} - P_{l+1})}{2l+1} \tag{68}$$

Expanding (66) in spherical harmonics and using the identities above we obtain,

$$\begin{aligned}
\vec{a} \cdot \vec{\nabla}_v f &= a \left(\frac{\partial}{\partial v} \cos[\theta] \sum_l f_l P_l[\cos[\theta]] + \frac{\sin^2[\theta]}{v} \frac{\partial}{\partial \cos[\theta]} \sum_l f_l P_l[\cos[\theta]] \right) \\
&= a \left[\sum_l \frac{\partial f_l}{\partial v} \left(\frac{(l+1)P_{l+1} + lP_{l-1}}{2l+1} \right) + \sum_l \frac{f_l}{v} \left(\frac{l(l+1)(P_{l-1} - P_{l+1})}{2l+1} \right) \right] \quad (69)
\end{aligned}$$

Since the summations are infinite, we are again free to re-index them, and solve for the zeroth and first order terms.

$$\begin{aligned}
\vec{a} \cdot \vec{\nabla}_v f &= a \left[\sum_l P_l \left\{ \frac{\partial f_{l-1}}{\partial v} \frac{l}{2l-1} + \frac{\partial f_{l+1}}{\partial v} \frac{l+1}{2l+3} + \frac{f_{l+1}}{v} \frac{(l+1)(l+2)}{2l+3} - \frac{f_{l-1}}{v} \frac{l(l-1)}{2l-1} \right\} \right] \\
&= a \left[\frac{1}{3} \frac{\partial f_1}{\partial v} + \frac{2}{3} \frac{f_1}{v} + \frac{\partial f_0}{\partial v} \cos[\theta] \right] \\
&= a \left[\frac{1}{3v^2} \frac{\partial(v^2 f_1)}{\partial v} + \frac{\partial f_0}{\partial v} \cos[\theta] \right] \quad (70)
\end{aligned}$$

Recalling that \vec{f}_1 is a vector, the final result for the energy flux is,

$$\vec{a} \cdot \vec{\nabla}_v f = \frac{1}{3v^2} \frac{\partial(v^2 \vec{a} \cdot \vec{f}_1)}{\partial v} + \frac{\vec{a} \cdot \vec{v}}{v} \frac{\partial f_0}{\partial v} \quad (71)$$

The final term in (56) is the collision integral. As first shown by Holstein [10, pp 368-372], this has two components: the contribution from elastic collisions and those from inelastic collisions. Following his derivation we arrive at an equation for each component.

$$\left(\frac{\partial f}{\partial t} \right)_{\text{elastic collisions}} = -Nv \cos[\theta] f_1 Q^{\text{elas}}[v] + \frac{N}{v^2} \frac{m}{M} \frac{\partial}{\partial v} (v^4 f_0 Q^{\text{elas}}[v]) \quad (72)$$

$$\left(\frac{\partial f}{\partial t} \right)_{\text{inelastic collisions}} = \sum_l N_l v \left(f_0[v'_l] \left(\frac{v'_l}{v} \right)^2 Q_l^{\text{inelas}}[v'_l] - f_0[v] Q_l^{\text{inelas}}[v] - \vec{f}_1[v] \cos[\theta] Q_l^{\text{inelas}}[v] \right) \quad (73)$$

where Q refers to the cross sections for either elastic or inelastic collisions, and l to a specific inelastic process. N is the colliding partner number density, v the velocity for

which the distribution function is being solved, i.e. $f_0[r, v]$, and v'_l a different velocity at which a specific inelastic collision l is taking place.

All of the terms are now combined by substituting (61), (71), (72), and (73) into (56). After moving to cylindrical coordinates, and expressing the dot product using $\cos[\theta]$, the Boltzmann equation in steady state becomes

$$\begin{aligned} v \cos[\theta] \frac{\partial f_0}{\partial r} + \frac{v}{3} \frac{1}{r} \frac{\partial}{\partial r} (r f_r) + \frac{1}{3v^2} \frac{\partial}{\partial v} (v^2 \vec{a} \cdot \vec{f}_1) + a \cos[\theta] \frac{\partial f_0}{\partial v} = \quad (74) \\ - N v \cos[\theta] \vec{f}_1 Q^{elas}[v] + \frac{N}{v^2} \frac{m}{M} \frac{\partial}{\partial v} (v^4 f_0 Q^{elas}[v]) \\ + \sum_l N_l v \left(f_0[v'_l] \left(\frac{v'_l}{v} \right)^2 Q_l^{inelas}[v'_l] - f_0[v] Q_l^{inelas}[v] - \vec{f}_1[v] \cos[\theta] Q_l^{inelas}[v] \right) \end{aligned}$$

We can split the above equation into three parts by first integrating over θ to remove the $\cos[\theta]$ terms; this gives (75). Next we multiply (74) by $\cos[\theta]$ and again integrate over θ ; this removes those terms without a $\cos[\theta]$. The resulting equation is further divided into two parts corresponding to the two terms in \vec{f}_1 , giving (76) and (77).

$$\begin{aligned} \frac{v}{3} \frac{1}{r} \frac{\partial}{\partial r} (r f_r) + \frac{1}{3v^2} \frac{\partial}{\partial v} (v^2 \vec{a} \cdot \vec{f}_1) \\ - \frac{N}{v^2} \frac{m}{M} \frac{\partial}{\partial v} (v^4 f_0 Q^{elas}[v]) - \sum_l N_l v \left(f_0[v'_l] \left(\frac{v'_l}{v} \right)^2 Q_l^{inelas}[v'_l] - f_0[v] Q_l^{inelas}[v] \right) = 0 \quad (75) \end{aligned}$$

$$v \frac{\partial f_0}{\partial r} + a_r \frac{\partial f_0}{\partial v} + N v f_r Q^{elas}[v] + \sum_l N v f_r Q_l^{inelas}[v] = 0 \quad (76)$$

$$a_z \frac{\partial f_0}{\partial v} + N v f_z Q^{elas}[v] + \sum_l N v f_z Q_l^{inelas}[v] = 0 \quad (77)$$

The next step is to change variables from velocity, v , to kinetic energy, u . At this time we also include the form of the acceleration given by $\vec{a} = -\frac{e_o}{m} \vec{E}$. With these

changes, the three equations (75)-(77) become,

$$\frac{u}{3r} \frac{\partial}{\partial r} (rf_r) - \frac{e_o}{3} \frac{\partial}{\partial u} [u(E_r[r]f_r + E_z f_z)] - \frac{\partial}{\partial u} [G[r, u]f_0] + uH[r, u]f_0 = S_0[r, u, f_0] \quad (78)$$

$$\frac{\partial f_0}{\partial r} - e_o E_r[r] \frac{\partial f_0}{\partial u} + K[r, u]f_r = 0 \quad (79)$$

$$-e_o E_z \frac{\partial f_0}{\partial u} + K[r, u]f_z = 0 \quad (80)$$

Where the new terms below follow the formalism of Uhrlandt and Winkler [7], and are fully described in section 3.1.

$$G[r, u] \equiv \sum_k 2 \frac{m}{M_k} u^2 N_k Q_k^{el}[u] \quad (81)$$

$$H[r, u] \equiv \sum_k \sum_l N_k Q_{kl}^{ex}[u] + \sum_k \sum_l N_k Q_{kl}^{de}[u] + \sum_k N_k Q_k^{io}[u] \quad (82)$$

$$K[r, u] \equiv \sum_k N_k Q_k^{el}[u] + H[r, u] \quad (83)$$

$$S_0[r, u, f_0] \equiv \sum_k \sum_l u'_l N_k Q_{kl}^{inelas}[u'_l] f_0[r, u'_l] \quad (84)$$

In writing (81)-(84) we have anticipated the need to consider more than one neutral species, which leads to the summation over k . The S_0 term shown is simplified from the one in equation (17). Where that equation is specific about the types of inelastic processes considered; equation (84) is more general.

The next step is another change of variables, this time from kinetic energy, u to the total energy $\epsilon[r]$. The total energy is a function of r because of the radial electric field. The relationship is

$$\varepsilon[r] = u - e_o V[r] \quad (85)$$

$$V[r] = - \int_0^r E_r[r] dr \quad (86)$$

With this transformation, the distributions are functions of ε , and we adopt the tilde to differentiate the two forms.

$$f_x[r, u[r, \varepsilon]] = \tilde{f}_x[r, \varepsilon] \quad (87)$$

$$\frac{\partial}{\partial r} f_x = \frac{\partial}{\partial r} \tilde{f}_x + e_o E_r[r] \frac{\partial}{\partial \varepsilon} \tilde{f}_x \quad (88)$$

$$\frac{\partial}{\partial u} f_x = \frac{\partial}{\partial \varepsilon} \tilde{f}_x \quad (89)$$

where x can refer to θ , r , or z .

With the transformation to total energy, equations (79) and (80) are solved for \tilde{f}_r and \tilde{f}_z respectively to give

$$\tilde{f}_r[r, \varepsilon] = - \frac{1}{K[r, \varepsilon]} \frac{\partial}{\partial r} \tilde{f}_0[r, \varepsilon] \quad (90)$$

$$\tilde{f}_z[r, \varepsilon] = \frac{e_o E_z}{K[r, \varepsilon]} \frac{\partial}{\partial \varepsilon} \tilde{f}_0[r, \varepsilon] \quad (91)$$

We then use (90) and (91) to eliminate \tilde{f}_r and \tilde{f}_z from (78). The result is the elliptic partial differential equation,

$$\frac{1}{r} \frac{\partial}{\partial r} \left(\frac{ru}{3K[r, \varepsilon]} \frac{\partial}{\partial r} \tilde{f}_0 \right) + \frac{\partial}{\partial \varepsilon} \left(\frac{u(e_o E_z)^2}{3K[r, \varepsilon]} \frac{\partial}{\partial \varepsilon} \tilde{f}_0 \right) + \frac{\partial}{\partial \varepsilon} (G[r, \varepsilon] \tilde{f}_0) - uH[r, \varepsilon] \tilde{f}_0 + \tilde{S}_0[r, \varepsilon, \tilde{f}_0] = 0 \quad (92)$$

This is the equation used in the strict solution.

Appendix C Derivation of Upper Boundary Condition

This appendix derives an approximate EEDF based on a limiting form of equation (10), valid at high energies. The resulting solution is used as an upper boundary condition for $\tilde{f}_0[r, \varepsilon_\infty]$; this boundary condition is discussed further in section 3.1.3 page 26.

The derivation begins with the strict kinetic CBE,

$$\frac{1}{r} \frac{\partial}{\partial r} \left(\frac{ru}{3K[r, \varepsilon]} \frac{\partial}{\partial r} \tilde{f}_0 \right) + \frac{\partial}{\partial \varepsilon} \left(\frac{u(e_o E_z)^2}{3K[r, \varepsilon]} \frac{\partial}{\partial \varepsilon} \tilde{f}_0 \right) + \frac{\partial}{\partial \varepsilon} (G[r, \varepsilon] \tilde{f}_0) - uH[r, \varepsilon] \tilde{f}_0 + \tilde{S}_0[r, \varepsilon, \tilde{f}_0] = 0 \quad (93)$$

At the highest energies the system is approximated by a balance between the field driven flux and the losses from inelastic collisions. The equation takes the form

$$\frac{\partial}{\partial \varepsilon} \left(\frac{u(e_o E_z)^2}{3K[r, \varepsilon]} \frac{\partial}{\partial \varepsilon} \tilde{f}_0 \right) = uH[r, \varepsilon] \tilde{f}_0 \quad (94)$$

We assume an EEDF of the form $\tilde{f}_0 = \alpha \exp[-\beta u]$, substitute this into (94), and expand the result.

$$\begin{aligned} \frac{\partial}{\partial \varepsilon} \left(\frac{u}{K[r, \varepsilon]} (-\beta) \tilde{f}_0 \right) &= \frac{3uH[r, \varepsilon]}{(e_o E_z)^2} \tilde{f}_0 \\ \tilde{f}_0 \left(\frac{\beta^2 u}{K[r, \varepsilon]} - \beta \frac{\partial}{\partial \varepsilon} \left(\frac{u}{K[r, \varepsilon]} \right) \right) &= \end{aligned} \quad (95)$$

To continue, we must assume a functional form for the inelastic cross section. In the case of neon, assume a weak dependence, $Q[u] = Q_0 u^{1/3}$. Then

$$\frac{\partial}{\partial \varepsilon} \left(\frac{u}{K[r, \varepsilon]} \right) \equiv \frac{\partial}{\partial \varepsilon} \left(\frac{u}{NQ[u]} \right) = \frac{\partial}{\partial \varepsilon} \left(\frac{u^{2/3}}{NQ_0} \right) = \frac{2}{3u^{1/3}NQ_0} \equiv \frac{2}{3K[r, \varepsilon]} \quad (96)$$

After substituting back into (95), solve for β .

$$\begin{aligned}
\tilde{f}_0 \left[\frac{\beta^2 u}{K[r, \epsilon]} - \frac{2\beta}{3K[r, \epsilon]} \right] &= \frac{3uH[r, \epsilon]}{(e_o E_z)^2} \tilde{f}_0 \\
\frac{\tilde{f}_0 \beta}{K[r, \epsilon]} [\beta u - 2/3] &= \\
\frac{\tilde{f}_0 \beta^2 u}{K[r, \epsilon]} &= \\
\beta^2 &= \frac{3}{(e_o E_z)^2} K[r, \epsilon] H[r, \epsilon]
\end{aligned} \tag{97}$$

where the term $2/3$ is dropped by assuming it is small in comparison to βu . A quick check of this assumption is appropriate. For typical values in a Neon discharge,

$$\begin{aligned}
\text{Neutral density} &\sim 2 \cdot 10^{16} \text{ cm}^{-3} & Q^{\text{elastic}} &\sim 3 \cdot 10^{-16} \text{ cm}^2 \\
E_z &\sim 2 \text{ V/cm} & Q^{\text{inelastic}} &\sim 1.4 \cdot 10^{-17} \text{ cm}^2 \\
u_{\text{max}} &\sim 30 \text{ eV}
\end{aligned}$$

$\beta \sim 0.4$, and thus $\beta u \sim 12.0$, which justifies the earlier assumption.

Based on the earlier assumed form for the distribution, $\tilde{f}_0 = \alpha \exp[-\beta u]$, we can relate $f_0[r, j_{\text{max}}]$ to $f_0[r, j_{\text{max}} - 1]$, where j signifies an energy bin counter. To simplify the expression assume $\beta[u]$ does not vary between $j_{\text{max}} - 1$ and j_{max} , then

$$\begin{aligned}
\tilde{f}_0[r, j_{\text{max}}] &= A \tilde{f}_0[r, j_{\text{max}} - 1] \\
A &= \exp[-\beta (u_{j_{\text{max}}} - u_{j_{\text{max}} - 1})] \\
\beta &= \sqrt{\frac{3}{(e_o E_z)^2} K[r, \epsilon_{\text{max}}] H[r, \epsilon_{\text{max}}]}
\end{aligned} \tag{98}$$

Appendix D Boltzmann Equation in Finite Differenced Form

Finite differencing begins with the analytic CBE derived in Appendix B,

$$\frac{1}{r} \frac{\partial}{\partial r} \left(\frac{ru}{3K[r, \varepsilon]} \frac{\partial}{\partial r} \tilde{f}_0 \right) + \frac{\partial}{\partial \varepsilon} \left(\frac{u(e_o E_z)^2}{3K[r, \varepsilon]} \frac{\partial}{\partial \varepsilon} \tilde{f}_0 \right) + \frac{\partial}{\partial \varepsilon} (G[r, \varepsilon] \tilde{f}_0) - uH[r, \varepsilon] \tilde{f}_0 + \tilde{S}_0[r, \varepsilon, \tilde{f}_0] = 0 \quad (99)$$

For the computer implementation, we change notation slightly. The two functions $K[r, \varepsilon]$ and $H[r, \varepsilon]$ are given descriptive names, $mtr[r, \varepsilon]$ and $inelas[r, \varepsilon]$ respectively (see discussion in section 3.1.1). Furthermore, let $\tilde{f}_0 \rightarrow f$, to ease the notation. With these changes, rewrite (99) as,

$$\frac{1}{r} \frac{\partial}{\partial r} (r\hat{H}[r, \varepsilon] \frac{\partial}{\partial r} f) + \frac{\partial}{\partial \varepsilon} (D[r, \varepsilon] \frac{\partial}{\partial \varepsilon} f) + \frac{\partial}{\partial \varepsilon} (G[r, \varepsilon] f) - u inelas[r, \varepsilon] f + \tilde{S}_0[r, \varepsilon, f] = 0 \quad (100)$$

where

$$\hat{H}[r, \varepsilon] \equiv \frac{u}{3mtr[r, \varepsilon]} \quad (101)$$

$$D[r, \varepsilon] \equiv \frac{u(e_o E_z)^2}{3mtr[r, \varepsilon]} \quad (102)$$

Now tackle the terms in (100) individually. First the radial flux term,

$\frac{1}{r} \frac{\partial}{\partial r} (r\hat{H}[r, \varepsilon] \frac{\partial}{\partial r} \tilde{f}_0)$. Using the differencing equations (36)-(40), we write this as

$$\frac{1}{r} \frac{\partial}{\partial r} (r\hat{H}[r, \varepsilon] \frac{\partial}{\partial r} f) \cong T_{i,j} f_{i+1,j} - (T_{i,j} + S_{i,j}) f_{i,j} + S_{i,j} f_{i-1,j} \quad (103)$$

$$T_{i,j} \equiv \frac{B_i^2}{r_i} \left(\alpha_i (2 + \alpha_i) r_{i+1} \hat{H}_{i+1,j} + (1 - \alpha_i^2) r_i \hat{H}_{i,j} + r_{i-1} \hat{H}_{i-1,j} \right)$$

$$S_{i,j} \equiv \frac{B_i^2}{r_i} \left(r_{i+1} \hat{H}_{i+1,j} + (1 - \beta_i^2) r_i \hat{H}_{i,j} + \beta_i (2 + \beta_i) r_{i-1} \hat{H}_{i-1,j} \right)$$

Next the energy terms, using modified forms of (36)-(40):

$$\frac{\partial}{\partial \varepsilon} (D[r, \varepsilon] \frac{\partial}{\partial \varepsilon} f) \equiv W_{i,j} f_{i,j+1} - (Y_{i,j} + W_{i,j}) f_{i,j} + Y_{i,j} f_{i,j-1} \quad (104)$$

$$W_{i,j} \equiv C_j^2 (\gamma_j (2 + \gamma_j) D_{i,j+1} + (1 - \gamma_j^2) D_{i,j} + D_{i,j-1})$$

$$Y_{i,j} \equiv C_j^2 (D_{i,j+1} + (1 - \delta_j^2) D_{i,j} + \delta_j (2 + \delta_j) D_{i,j-1})$$

and

$$\frac{\partial}{\partial \varepsilon} (G[r, \varepsilon] \tilde{f}_0) \equiv K_{i,j} f_{i,j+1} + (N_{i,j} - L_{i,j}) f_{i,j} + M_{i,j} f_{i,j-1} \quad (105)$$

$$K_{i,j} \equiv C_j \gamma_j G_{i,j+1}$$

$$M_{i,j} \equiv C_j \delta_j G_{i,j-1}$$

$$L_{i,j} \equiv C_j \gamma_j G_{i,j}$$

$$N_{i,j} \equiv C_j \delta_j G_{i,j}$$

As the last two terms of (100) don't involve any derivatives, they are evaluated simply at each i, j . The equations given above form the complete set for all interior points on the grid. At the boundaries we must use forward or backward differencing, and consider the boundary conditions.

Start first with the $r = 0$ boundary. Note that the only term that needs modification is the radial flux term, since as (103) is written, it tries to access a point $f_{i-1,j}$ outside of the grid. To fix this we first take the limit of the radial flux as $r \rightarrow 0$,

$$\frac{1}{r} \frac{\partial}{\partial r} (r \hat{H}[r, \varepsilon] \frac{\partial}{\partial r} f) \Big|_{r \rightarrow 0} = 2 \hat{H}[r, \varepsilon] \frac{\partial^2 f}{\partial r^2} \Big|_{r=0} \quad (106)$$

Since we are on the edge of the grid, invent a hypothetical grid point at $i = -1$ and assume uniform grid spacing, then $\frac{\partial^2 f}{\partial r^2}$ becomes

$$\frac{\partial^2 f}{\partial r^2} \equiv \frac{f_{i-1,j} - 2f_{i,j} + f_{i+1,j}}{\Delta r^2} \quad (107)$$

Use the $r = 0$ boundary condition

$$\begin{aligned}
\left. \frac{\partial f}{\partial r} \right|_{r=0} &= 0 \cong \frac{f_{1,j} - f_{-1,j}}{2r_1} \\
\therefore f_{1,j} &= f_{-1,j} \\
2\hat{H}[r, \varepsilon] \left. \frac{\partial^2 f}{\partial r^2} \right|_{r=0} &\cong \frac{4H_{0,j}(f_{1,j} - f_{0,j})}{r_1^2}
\end{aligned} \tag{108}$$

At the next boundary, $u = 0$, directly enforce the boundary condition given in (19). The condition is

$$(e_o E_z)^2 \left. \frac{\partial f}{\partial \varepsilon} \right|_{u=0} - e_o \left. \frac{\partial \phi[r]}{\partial r} \frac{\partial f}{\partial r} \right|_{u=0} = 0 \tag{109}$$

where $\phi[r] = -V[r]$. Since both derivatives involve the boundary, neither can be treated with central differencing. Instead, employ backward differencing for the radial derivative, and forward for the energy derivative. As discussed in section 3.2.3, we have made a decision to limit our radial increments to ± 1 around these solution points, in order to speed the solution. This forces us to use a two-point derivative in the radial direction, while for the energy derivative we are free to use equation (37). The resulting differenced equations are

$$\begin{aligned}
0 &\cong -R1_i f_{i,j} + R2_i f_{i,j+1} - R3_i f_{i,j+2} + R4_i f_{i-1,j} \\
R1_i &\equiv \left(\left. \frac{\partial \phi}{\partial r} \right|_i \frac{1}{(r_i - r_{i-1})} + E_z^2 C_{i+1} (\delta_{i+1} + 2) \right) \\
R2_i &\equiv E_z^2 C_{i+1} (\gamma_{i+1} + \delta_{i+1} + 2) \\
R3_i &\equiv E_z^2 C_{i+1} \gamma_{i+1} \\
R4_i &\equiv \left. \frac{\partial \phi}{\partial r} \right|_i \frac{1}{(r_i - r_{i-1})}
\end{aligned} \tag{110}$$

There is a special point at the origin where both the $r = 0$ and $u = 0$ boundary conditions hold. At this point $\frac{\partial f}{\partial r} = 0$ and (110) reduces to

$$\begin{aligned} 0 &\equiv -Q1_0 f_{0,0} + Q2_0 f_{0,1} - Q3_0 f_{0,2} \\ Q1_0 &\equiv E_z^2 C_1 (\delta_1 + 2) \\ Q2_0 &\equiv E_z^2 C_1 (\gamma_1 + \delta_1 + 2) \\ Q3_0 &\equiv E_z^2 C_1 \gamma_1 \end{aligned} \quad (111)$$

At the wall boundary, similar to the $r = 0$ boundary, only the radial equation needs alteration. The technique is to substitute for $f_{i+1,j}$ in equation (103) with a discrete version of whatever wall loss condition is used. In the case of the wall loss function, this leads to

$$\begin{aligned} \frac{1}{r} \frac{\partial}{\partial r} (r \hat{H}[r, \varepsilon] \frac{\partial}{\partial r} f) &\equiv T_{i,j} F_{i,j} - (T_{i,j} + S_{i,j}) f_{i,j} + (T_{i,j} + S_{i,j}) f_{i-1,j} \\ F_{i,j} &\equiv -2(r_i - r_{i-1}) \text{mtr}[r_i, \varepsilon_{i,j}] A \exp[au_{i,j}^2] \end{aligned} \quad (112)$$

where A and a are input parameters as shown in equation (21).

For the wall loss cone, the radial flux becomes

$$\begin{aligned} \frac{1}{r} \frac{\partial}{\partial r} (r \hat{H}[r, \varepsilon] \frac{\partial}{\partial r} f) &\equiv -(T_{i,j} X_{i,j} + T_{i,j} + S_{i,j}) f_{i,j} + (T_{i,j} + S_{i,j}) f_{i-1,j} \\ X_{i,j} &\equiv 2(r_i - r_{i-1}) \text{mtr}[r_i, \varepsilon_{i,j}] \frac{3(1-\chi)}{2(1+\chi)} \end{aligned}$$

When $j = NJ-1$, we substitute into (104) and (105) for $f_{i,j+1}$. Using equation (20), the energy flux terms become

$$\frac{\partial}{\partial \varepsilon} (D[r, \varepsilon] \frac{\partial}{\partial \varepsilon} f) \cong (W_{i,j} AA - Y_{i,j} - W_{i,j}) f_{i,j} + Y_{i,j} f_{i,j-1} \quad (113)$$

$$\frac{\partial}{\partial \varepsilon} (G[r, \varepsilon] \tilde{f}_0) \cong (K_{i,j} AA + N_{i,j} - L_{i,j}) f_{i,j} + M_{i,j} f_{i,j-1} \quad (114)$$

where

$$AA = \exp[-\beta (u_{j_{\max}} - u_{j_{\max}-1})] \quad (115)$$

$$\beta = \sqrt{\frac{3}{(e_o E_z)^2} mtr[r, \varepsilon_{\max}] inelas[r, \varepsilon_{\max}]}$$

This completes the set of differenced equations.

Bibliography

- 1 Hilbun, William M. "Shock Waves in Nonequilibrium Gases and Plasmas," Doctoral Dissertation, Air Force Institute of Technology, 1997.
- 2 Ganguly, B. N. and Bletzinger, P. "Shock Wave Dispersion in Nonequilibrium Plasmas," *AIAA Paper* 96-4607 (1996).
- 3 Ganguly, B. N., Bletzinger, P., and Garscadden, A. "Shock Wave Damping and Dispersion in Nonequilibrium Low Pressure Argon Plasmas," *Physics Letters A*, **230**(3-4):218-222 (1997).
- 4 Nasser, E. *Fundamentals of Gaseous Ionization and Plasma Electronics*. New York: John Wiley & Sons, 1971.
- 5 Howatson, A. M. *An Introduction to Gas Discharges*. New York: Pergamon Press, 1976.
- 6 Bennett, E. J. (Private Communication, 1998), Bennett provided the author with models that implement the local and nonlocal approximations as well as a derivation of the nonlocal equation set. In addition we borrow from his discussion of the basic physics underlying the Glow Discharge.
- 7 Uhrlandt, D. and Winkler, R. "Radial Structure of the Kinetics and Production of Electrons in the dc Column Plasma," *Plasma Chemistry and Plasma Processing*, **16**(4):517-545 (1996).
- 8 Ingold, J.H. "Nonequilibrium Positive Column," *Physical Review E*, **56**(5):5932-5944 (November 1997).
- 9 Kortshagen, U., *et al.* "Comparison of Monte Carlo Simulations and Nonlocal Calculations of the Electron Distribution Function in a Positive Column Plasma," *Physical Review E*, **54**(6):6746-6761 (December 1996).
- 10 Holstein, T. "Energy Distribution of Electrons in High Frequency Gas Discharges," *Physical Review*, **70**(5): 367-384 (September 1946).
- 11 Rockwood, S. "Elastic and Inelastic Cross Sections for Electron-Hg Scattering from Hg Transport Data," *Physical Review A*, **8**(5):2348-2358 (November 1973).
- 12 Bernstein, I.B. and Holstein, T. "Electron Energy Distributions in Stationary Discharges," *Physical Review*, **94**(6):1475-1482 (June 1954).
- 13 *Electrons, Ions, and Waves: Selected Works of William Phelps Allis*. Cambridge: MIT Press, 1967, edited by S.C. Brown.

- 14 Kortshagen, U., Busch C., and Tsendin L.D. "On Simplifying Approaches to the Solution of the Boltzmann Equation in Spatially Inhomogeneous Plasmas," *Plasma Sources Sci. Technology*, **5**:1-17 (1996).
- 15 Bush, C. and Kortshagen, U. "Numerical Solution of the Spatially Inhomogeneous Boltzmann Equation and Verification of the Nonlocal Approach for an Argon Plasma," *Physical Review E*, **51**(1):280-288 (January 1995).
- 16 Uhrlandt, D. and Winkler, R. Poster presented at the *Gaseous Electronics Conference*, Madison, WI, 5-9 October 1997.
- 17 Alves, L.L., Gousset, G., and Ferreira, C.M. "Self-Contained Solution to the Spatially Inhomogeneous Electron Boltzmann Equation in a Cylindrical Plasma Positive Column," *Physical Review E*, **55**(1):890-906 (January 1997).
- 18 Tsendin, L. D. and Golubovskii, Y. B. "Positive Column of a Low Density, Low Pressure Discharge. I. Electron Energy Distribution," *Soviet Physics Technical Physics*, **22**(9):1066-1073 (1977).
- 19 Burden, Richard L. and Faires J. Douglas, *Numerical Analysis*, New York, Brooks/Cole Publishing Company, 1997.
- 20 Uhrlandt, D. and Winkler, R. "Radially Inhomogeneous Electron Kinetics in the DC Column Plasma," *J Phys D: Apply Phys*, **29**:115-120 (1996).
- 21 Allis, W.P. *Handbuch der Physik*, Berlin: Springer-Verlag, 1956, Vol. XXI

Vita

Captain Christopher G. Smithtro was born on 5 July 1969 in Phoenix, Arizona. He graduated from Adolfo Camarillo High School in 1987, and attended Harvey Mudd College in Claremont, California where he graduated with a Bachelor of Science degree in Physics in May 1991. Captain Smithtro received his commission through Detachment 060 AFROTC at the University of Southern California where he was recognized as a Distinguished Graduate. His first assignment was to the Air Force Institute of Technology, Basic Meteorology Program at Florida State University in Tallahassee, Florida. After completion of this assignment, Captain Smithtro was transferred to Ellsworth AFB in Rapid City, South Dakota where he served as the Wing Weather Officer for the 28th Bomb Wing and 44th Missile Wing. He later moved to Hurlburt Field in Fort Walton Beach, Florida, serving first as the Officer-In-Charge, Special Operations Weather Team and later as the Weather Flight Commander for the 16th Special Operations Wing. He entered the School of Engineering, Air Force Institute of Technology in August of 1997 to pursue a Master of Science degree in Applied Physics, and was invited to join the Tau Beta Pi Honor Society. Upon graduation, he will be assigned to the 55th Space Weather Squadron. Captain Smithtro is married to Lieutenant Sally A. Richmond.

Permanent Address: 2142 Klamath Dr.
Camarillo, CA 93010

REPORT DOCUMENTATION PAGE			Form Approved OMB No. 0704-0188	
Public reporting burden for this collection of information is estimated to average 1 hour per response, including the time for reviewing instructions, searching existing data sources, gathering and maintaining the data needed, and completing and reviewing the collection of information. Send comments regarding this burden estimate or any other aspect of this collection of information, including suggestions for reducing this burden, to Washington Headquarters Services, Directorate for Information Operations and Reports, 1215 Jefferson Davis Highway, Suite 1204, Arlington, VA 22202-4302, and to the Office of Management and Budget, Paperwork Reduction Project (0704-0188), Washington, DC 20503.				
1. AGENCY USE ONLY (Leave blank)	2. REPORT DATE March 1999	3. REPORT TYPE AND DATES COVERED		
4. TITLE AND SUBTITLE Numerical Solutions to the Two Dimensional Boltzmann Equation		5. FUNDING NUMBERS None		
6. AUTHOR(S) Christopher G. Smithtro, Capt, USAF				
7. PERFORMING ORGANIZATION NAME(S) AND ADDRESS(ES) AFIT/ENP 2950 P. St. Wright-Patterson AFB, OH 45433 Advisor: William F. Bailey, COMM: (937) 255-3636 ext 4501 Email: william.bailey@afit.af.mil		8. PERFORMING ORGANIZATION REPORT NUMBER AFIT/GAP/ENP/99M-13		
9. SPONSORING/MONITORING AGENCY NAME(S) AND ADDRESS(ES) AFRL/PR, Air Force Research Laboratory, Propulsion Directorate Bldg 18 1950 Fifth St. WPAFB, OH 45433-7251 Dr. Alan Garscadden COMM 937-255-2246		10. SPONSORING/MONITORING AGENCY REPORT NUMBER		
11. SUPPLEMENTARY NOTES				
12a. DISTRIBUTION AVAILABILITY STATEMENT Approved for public release; distribution unlimited			12b. DISTRIBUTION CODE	
13. ABSTRACT (Maximum 200 words) A strict kinetic, two-dimensional model of the electron kinetics within a glow discharge positive column is developed. The problem is solved in cylindrical geometry using the standard two-term Legendre expansion of the electron velocity distribution function. The model establishes a steady state solution, such that the net ionization rate is exactly balanced by the wall loss. In addition to a thorough analytic development, we present the numerical techniques used to solve the resulting elliptic partial differential equation, including an efficient method to treat sparse banded matrices. The model is validated against published results, local and nonlocal kinetic approximations, and a previous Monte Carlo treatment. Having created a working model, we conduct an investigation into current flow within the solution area of a neon column, made possible by this 2-D treatment. Furthermore, we investigate the range of applicability of the earlier local and nonlocal kinetic approximations and finally present a short discussion on the effect different forms of wall loss have on the overall distribution function.				
14. SUBJECT TERMS Boltzmann Equation, Glow Discharge, Positive Column, Non-equilibrium Weakly Ionized Gases			15. NUMBER OF PAGES 109	
			16. PRICE CODE	
17. SECURITY CLASSIFICATION OF REPORT Unclassified	18. SECURITY CLASSIFICATION OF THIS PAGE Unclassified	19. SECURITY CLASSIFICATION OF ABSTRACT Unclassified	20. LIMITATION OF ABSTRACT UL	